

1 **Virological characteristics of SARS-CoV-2 BA.2 variant**

2

3 Daichi Yamasoba<sup>1,2,31</sup>, Izumi Kimura<sup>1,31</sup>, Hesham Nasser<sup>3,4,31</sup>, Yuhei Morioka<sup>5,31</sup>,  
4 Naganori Nao<sup>6,7,31</sup>, Jumpei Ito<sup>1,31</sup>, Keiya Uriu<sup>1,8,31</sup>, Masumi Tsuda<sup>9,10,31</sup>, Jiri  
5 Zahradnik<sup>11,31</sup>, Kotaro Shirakawa<sup>12</sup>, Rigel Suzuki<sup>5</sup>, Mai Kishimoto<sup>13</sup>, Yusuke  
6 Kosugi<sup>1,14,15</sup>, Kouji Kobiyama<sup>16</sup>, Teppei Hara<sup>16</sup>, Mako Toyoda<sup>17</sup>, Yuri L Tanaka<sup>18</sup>,  
7 Erika P Butlertanaka<sup>18</sup>, Ryo Shimizu<sup>3</sup>, Hayato Ito<sup>5</sup>, Lei Wang<sup>9,10</sup>, Yoshitaka Oda<sup>9</sup>,  
8 Yasuko Orba<sup>13,19</sup>, Michihito Sasaki<sup>13,19</sup>, Kayoko Nagata<sup>12</sup>, Kumiko Yoshimatsu<sup>20</sup>,  
9 Hiroyuki Asakura<sup>21</sup>, Mami Nagashima<sup>21</sup>, Kenji Sadamasu<sup>21</sup>, Kazuhisa  
10 Yoshimura<sup>21</sup>, Jin Kuramochi<sup>22</sup>, Motoaki Seki<sup>23</sup>, Ryoji Fujiki<sup>23</sup>, Atsushi Kaneda<sup>23</sup>,  
11 Tadanaga Shimada<sup>24</sup>, Taka-aki Nakada<sup>24</sup>, Seiichiro Sakao<sup>25</sup>, Takuji Suzuki<sup>25</sup>,  
12 Takamasa Ueno<sup>17</sup>, Akifumi Takaori-Kondo<sup>12</sup>, Ken J Ishii<sup>16</sup>, Gideon Schreiber<sup>11</sup>,  
13 The Genotype to Phenotype Japan (G2P-Japan) Consortium, Hirofumi  
14 Sawa<sup>6,7,13,19</sup>, Akatsuki Saito<sup>18,26,27\*</sup>, Takashi Irie<sup>28\*</sup>, Shinya Tanaka<sup>9,10\*</sup>, Keita  
15 Matsuno<sup>7,19,29\*</sup>, Takasuke Fukuhara<sup>5\*</sup>, Terumasa Ikeda<sup>3\*</sup>, Kei Sato<sup>1,8,30\*</sup>.

16

17 <sup>1</sup> Division of Systems Virology, Department of Infectious Disease Control,  
18 International Research Center for Infectious Diseases, The Institute of Medical  
19 Science, The University of Tokyo, Tokyo, Japan.

20 <sup>2</sup> Faculty of Medicine, Kobe University, Kobe, Japan.

21 <sup>3</sup> Division of Molecular Virology and Genetics, Joint Research Center for Human  
22 Retrovirus infection, Kumamoto University, Kumamoto, Japan.

23 <sup>4</sup> Department of Clinical Pathology, Faculty of Medicine, Suez Canal University,  
24 Ismailia, Egypt.

25 <sup>5</sup> Department of Microbiology and Immunology, Graduate School of Medicine,  
26 Hokkaido University, Sapporo, Japan.

27 <sup>6</sup> Division of International Research Promotion, International Institute for  
28 Zoonosis Control, Hokkaido University, Sapporo, Japan.

29 <sup>7</sup> One Health Research Center, Hokkaido University, Sapporo, Japan.

30 <sup>8</sup> Graduate School of Medicine, The University of Tokyo, Tokyo, Japan.

31 <sup>9</sup> Department of Cancer Pathology, Faculty of Medicine, Hokkaido University,  
32 Sapporo, Japan.

33 <sup>10</sup> Institute for Chemical Reaction Design and Discovery (WPI-ICReDD),  
34 Hokkaido University, Sapporo, Japan.

35 <sup>11</sup> Department of Biomolecular Sciences, Weizmann Institute of Science,  
36 Rehovot, Israel.

37 <sup>12</sup> Department of Hematology and Oncology, Graduate School of Medicine,  
38 Kyoto University, Kyoto, Japan.

39 <sup>13</sup> Division of Molecular Pathobiology, International Institute for Zoonosis Control,  
40 Hokkaido University, Sapporo, Japan.

41 <sup>14</sup> Laboratory of Systems Virology, Institute for Frontier Life and Medical  
42 Sciences, Kyoto University, Kyoto, Japan.

43 <sup>15</sup> Graduate School of Pharmaceutical Sciences, Kyoto University, Kyoto, Japan.

44 <sup>16</sup> Division of Vaccine Science, Department of Microbiology and Immunology,  
45 The Institute of Medical Science, The University of Tokyo, Tokyo, Japan.

46 <sup>17</sup> Division of Infection and immunity, Joint Research Center for Human  
47 Retrovirus infection, Kumamoto University, Kumamoto, Japan

48 <sup>18</sup> Department of Veterinary Science, Faculty of Agriculture, University of  
49 Miyazaki, Miyazaki, Japan.

50 <sup>19</sup> International Collaboration Unit, International Institute for Zoonosis Control,  
51 Hokkaido University, Sapporo, Japan.

52 <sup>20</sup> Institute for Genetic Medicine, Hokkaido University, Sapporo, Japan.

53 <sup>21</sup> Tokyo Metropolitan Institute of Public Health, Tokyo, Japan.

54 <sup>22</sup> Kuramochi Clinic Interpark, Utsunomiya, Japan.

55 <sup>23</sup> Department of Molecular Oncology, Graduate School of Medicine, Chiba  
56 University, Chiba, Japan.

57 <sup>24</sup> Department of Emergency and Critical Care Medicine, Graduate School of  
58 Medicine, Chiba University, Chiba, Japan.

59 <sup>25</sup> Department of Respiriology, Graduate School of Medicine, Chiba University,  
60 Chiba, Japan.

61 <sup>26</sup> Center for Animal Disease Control, University of Miyazaki, Miyazaki, Japan.

62 <sup>27</sup> Graduate School of Medicine and Veterinary Medicine, University of Miyazaki,  
63 Miyazaki, Japan.

64 <sup>28</sup> Institute of Biomedical and Health Sciences, Hiroshima University, Hiroshima,  
65 Japan.

66 <sup>29</sup> Division of Risk Analysis and Management, International Institute for Zoonosis  
67 Control, Hokkaido University, Sapporo, Japan.

68 <sup>30</sup> CREST, Japan Science and Technology Agency, Saitama, Japan.

69 <sup>31</sup> These authors contributed equally: Izumi Kimura, Daichi Yamasoba, Hesham  
70 Nasser, Yuhei Morioka, Naganori Nao, Jumpei Ito, Keiya Uriu, Masumi Tsuda,  
71 Jiri Zahradnik.

72

73 \*Corresponding authors:

74 sakatsuki@cc.miyazaki-u.ac.jp (Akatsuki Saito);

75 tirie@hiroshima-u.ac.jp (Takashi Irie);

76 tanaka@med.hokudai.ac.jp (Shinya Tanaka);

77 matsuk@czc.hokudai.ac.jp (Keita Matsuno);

78 fukut@pop.med.hokudai.ac.jp (Takasuke Fukuhara);

79 ikedat@kumamoto-u.ac.jp (Terumasa Ikeda);

80 KeiSato@g.ecc.u-tokyo.ac.jp (Kei Sato)

81

82 **Keywords:**

83 SARS-CoV-2; COVID-19; Omicron; BA.2; BA.1; B.1.1.529; pathogenicity;  
84 fusogenicity; transmissibility

85 **Abstract**

86 Soon after the emergence and global spread of a new severe acute respiratory  
87 syndrome coronavirus 2 (SARS-CoV-2) Omicron lineage, BA.1 (ref<sup>1,2</sup>), another  
88 Omicron lineage, BA.2, has initiated outcompeting BA.1. Statistical analysis  
89 shows that the effective reproduction number of BA.2 is 1.4-fold higher than that  
90 of BA.1. Neutralisation experiments show that the vaccine-induced humoral  
91 immunity fails to function against BA.2 like BA.1, and notably, the antigenicity of  
92 BA.2 is different from BA.1. Cell culture experiments show that BA.2 is more  
93 replicative in human nasal epithelial cells and more fusogenic than BA.1.  
94 Furthermore, infection experiments using hamsters show that BA.2 is more  
95 pathogenic than BA.1. Our multiscale investigations suggest that the risk of BA.2  
96 for global health is potentially higher than that of BA.1.

## 97 **Introduction**

98 Virological characteristics of newly emerging SARS-CoV-2 variants, such as  
99 transmissibility, pathogenicity and resistance to the vaccine-induced immunity  
100 and antiviral drugs, is an urgent global health concern. In February 2022, the  
101 Omicron variant (B.1.1.529 and BA lineages) spreads worldwide and represents  
102 the most recently recognised variant of concern<sup>2</sup>. Omicron was first reported  
103 from South Africa at the end of November 2021<sup>1</sup>. Then, a variant of Omicron, the  
104 BA.1 lineage, has rapidly spread worldwide and outcompeted other variants  
105 such as Delta.

106 As of February 2022, another variant of Omicron, the BA.2 lineage, has  
107 detected in multiple countries such as Denmark and UK<sup>3</sup>. Notably, BA.2 has  
108 initiated outcompeting BA.1<sup>3</sup>, suggesting that BA.2 is more transmissible than  
109 BA.1.

110 In a few months since the emergence of BA.1, we and others revealed  
111 the virological characteristics of BA.1<sup>4-19</sup>. For instance, BA.1 is highly resistant to  
112 the vaccine-induced humoral immunity and antiviral drugs<sup>4-11,16-19</sup>. Also, the  
113 spike (S) protein of BA.1 is less efficiently cleaved by furin and less fusogenic  
114 than those of Delta and an ancestral SARS-CoV-2 belonging to the B.1.1  
115 lineage<sup>11,12</sup>. Further, the pathogenicity of BA.1 is attenuated when compared to  
116 Delta and an ancestral B.1.1 virus<sup>12-14</sup>. However, the virological characteristics of  
117 BA.2 remains unaddressed.

118

## 119 **Phylogenetic and epidemic dynamics of BA.2**

120 As of February 2022, Omicron is classified into three main lineages, BA.1, BA.2,  
121 BA.3, and a sublineage of BA.1, BA1.1, which harbours the R346K substitution  
122 in S (**Fig. 1a**). Although these lineages are monophyletic, their sequences have  
123 been greatly diversified. For example, BA.1 differs from BA.2 by 50 amino acids,  
124 which is approximately twice as much as the numbers of amino acid differences  
125 between four VOCs (Alpha, Beta, Gamma and Delta) and Wuhan-Hu-1, a  
126 prototypic SARS-CoV-2 isolate (**Fig. 1b**). Phylodynamics analysis suggests that  
127 BA.1 emerged first, followed by BA.2 and BA.3 (**Extended Data Fig. 1**). In  
128 addition to BA.1, the earlier strains of BA.2, BA.3, and BA.1.1 were isolated from  
129 Gauteng Province, South Africa, the place of the earliest Omicron (BA.1)  
130 epidemic (**Extended Data Fig. 1**)<sup>20</sup>. These results suggest that the remarkable  
131 diversification of Omicron occurred in Gauteng Province and all Omicron  
132 lineages emerged there.

133 Although BA.1 spread worldwide earlier than BA.2, the lineage  
134 frequency of BA.2 increased and exceeded that of BA.1 since January 2022 in  
135 multiple countries, such as Philippines, India, Denmark, Singapore, Austria, and  
136 South Africa (**Fig. 1c and Extended Data Fig. 2**). To quantify the growth  
137 advantage of BA.2 in the human population, we constructed a Bayesian model

138 representing the epidemic dynamics of SARS-CoV-2 lineages. This hierarchical  
139 model can estimate the global average of the relative effective reproduction  
140 numbers of viral lineages (**Fig. 1d**) as well as those in each country (**Extended**  
141 **Data Fig. 2**). The effective reproduction number of BA.2 is 1.40-fold higher than  
142 that of BA.1 on average in the world [95% confidence interval (CI), 1.29–1.52;  
143 **Fig. 1d**]. Furthermore, the effective reproduction number of BA.2 was even  
144 higher than that of BA.1.1, which spread more rapidly than BA.1 in several  
145 countries such as the UK and USA (**Fig. 1d and Extended Data Fig. 2d**). These  
146 results suggest that the BA.2 epidemic will more expand around the world,  
147 raising the importance of elucidating virological features of BA.2 in depth.

148

### 149 **Immune resistance of BA.2**

150 Since the sequence of BA.2, particularly in S protein, is substantially different  
151 from that of BA.1 (**Fig. 1b and Fig. 2a**), it is reasonable to assume that the  
152 virological properties of BA.2, such as immune resistance and pathogenicity, are  
153 different from those of BA.1. To reveal the virological features of BA.2, we set  
154 out to perform neutralisation assay using pseudoviruses and the neutralising  
155 antibodies elicited by vaccination. Consistent with recent studies<sup>4-11,16-19</sup>, BA.1 is  
156 highly resistant to the antisera elicited by mRNA-1273 and ChAdOx1 vaccines  
157 (**Fig. 2b,c**). Similar to BA.1, BA.2 was also highly resistant to the  
158 vaccine-induced antisera (**Fig. 2b,c**). Also, BA.2 was almost completely  
159 resistant to two therapeutic monoclonal antibodies, Casirivimab and Imdevimab,  
160 and was 35-fold more resistant to another therapeutic antibody, Sotrovimab,  
161 when compared to the ancestral D614G-bearing B.1.1 virus (**Fig. 2d**). Moreover,  
162 both BA.1 and BA.2 were highly resistant to the convalescent sera who had  
163 infected with early pandemic virus (before May 2020; **Fig. 2e**), Alpha (**Extended**  
164 **data Fig. 3a**) and Delta (**Extended data Fig. 3b**). These data suggest that,  
165 similar to BA.1, BA.2 is highly resistant to the antisera induced by vaccination  
166 and infection with other SARS-CoV-2 variants as well as three antiviral  
167 therapeutic antibodies.

168 We then tested the 17 sera infected with BA.1: 13 convalescents were  
169 fully vaccinated (2 shots), 1 convalescent was 1-dose vaccinated, and 3  
170 convalescents were not vaccinated. BA.1 convalescent sera exhibited the  
171 strongest antiviral effect against BA.1 (**Fig. 2f**). Although BA.2 was 1.4-fold more  
172 resistant to the BA.1-infected sera than BA.1, there was no statistical difference  
173 (**Fig. 2f**;  $P=0.091$  by Wilcoxon signed-rank test). Importantly, the BA.1  
174 convalescent sera with full vaccination exhibited significantly stronger antiviral  
175 effects against all variants tested than unvaccinated or 1-dose vaccinated  
176 convalescents (**Extended Data Fig. 3c**).

177 To address the possibility that the BA.1-induced humoral immunity is  
178 less effective against BA.2, we used the convalescent sera obtained from

179 infected hamsters at 16 days postinfection (d.p.i.). Similar to the results of  
180 convalescent human sera (**Fig. 2e** and **Extended Data Fig. 2b**), both BA.1 and  
181 BA.2 exhibited pronounced resistances against B.1.1- and Delta-infected  
182 convalescent hamster sera (**Fig. 2g** and **Extended Data Fig. 3d**). Interestingly,  
183 BA.2 was significantly (2.9-fold) more resistant to BA.1-infected convalescent  
184 hamster sera than BA.1 (**Fig. 2g**). To further verify the resistance of BA.2  
185 against BA.1-induced immunity, mice were immunised with the cells expressing  
186 the S proteins of ancestral B.1.1 and BA.1 and obtained murine antisera. Again,  
187 the neutralisation assay using murine sera showed that BA.2 is more  
188 significantly (6.4-fold) resistant to the BA.1 S-immunised sera than BA.1 (**Fig.**  
189 **2h**). These findings suggest that BA.1-induced humoral immunity is less  
190 effective against BA.2.

191

### 192 **Virological features of BA.2 in vitro**

193 To investigate the virological characteristics of BA.2, we generated chimeric  
194 recombinant SARS-CoV-2 that expresses GFP and harbours the S gene of  
195 ancestral B.1.1, Delta, BA.1 and BA.2 by reverse genetics (**Extended Data Fig.**  
196 **4**)<sup>21</sup>. Although the growth of BA.1 and BA.2 was comparable in  
197 VeroE6/TMPRSS2 cells, BA.2 was more replicative than BA.1 in Calu-3 cells  
198 and primary human nasal epithelial cells (**Fig. 3a**). Notably, the morphology of  
199 infected cells was different; BA.2 formed significantly (1.52-fold) larger syncytia  
200 than BA.1 (**Fig. 3b** and **Extended Data Fig. 5a**). Whereas the plaque size in  
201 VeroE6/TMPRSS2 cells infected with BA.1 and BA.2 was significantly smaller  
202 than those of cells infected with B.1.1, the plaques formed by BA.2 infection are  
203 significantly (1.27-fold) larger than those by BA.1 infection (**Fig. 3c** and  
204 **Extended Data Fig. 5b**). Moreover, the coculture of S-expressing cells with  
205 HEK293-ACE2/TMPRSS2 cells showed that BA.2 S induces significantly  
206 (2.9-fold) larger multinuclear syncytia formation when compared to BA.1 S  
207 (**Extended Data Fig. 5c**). These data suggest that BA.2 is more fusogenic than  
208 BA.1. To further address this possibility, we analysed the fusogenicity of the S  
209 proteins of BA.2 S by a cell-based fusion assay<sup>12,22,23</sup>. The expression level of  
210 BA.2 S on the cell surface was significantly lower than that of BA.1 S (**Extended**  
211 **Data Fig. 6a**). Nevertheless, our fusion assay using VeroE6/TMPRSS2 cells and  
212 Calu-3 cells showed that BA.2 S is significantly more fusogenic than BA.1 S (**Fig.**  
213 **3d**). We then analysed the binding affinity of BA.2 S receptor binding domain  
214 (RBD) to ACE2 by a yeast surface display assay<sup>16,22,24</sup>. Although the binding  
215 affinity of BA.1 S RBD to ACE2 is controversial<sup>11,15-17,25,26</sup>, our yeast surface  
216 display showed that the binding affinity of the RBD of BA.1 and BA.2 is  
217 comparable (**Extended Data Fig. 6b**).

218 Because we have proposed that the SARS-CoV-2 S-mediated  
219 fusogenicity is closely associated with the efficacy of S1/S2 cleavage<sup>12,23</sup>, we

220 hypothesized that BA.2 S is more efficiently cleaved than BA.1 S. However, an  
221 western blotting analysis showed that BA.2 S is less cleaved than BA.1 S (**Fig.**  
222 **3e**), suggesting that BA.2 S exhibits a higher fusogenicity independently of  
223 S1/S2 cleavage.

224 We have recently revealed that BA.1 poorly utilizes TMPRSS2 for the  
225 infection<sup>11</sup>. To analyse the TMPRSS2 usage by BA.2 S, we performed  
226 cell-based fusion assay using 293-ACE2 cells with or without TMPRSS2  
227 expression. We verified that 293-ACE2 cells do not express endogenous  
228 TMPRSS2 on the cell surface (**Extended Data Fig. 6c**). As shown in **Fig. 3f**, the  
229 fusogenicity of BA.2 S was significantly higher in both cell lines than that of BA.1.  
230 However, although BA.2 S was less fusogenic than B.1.1 S in 293-ACE2 cells,  
231 the fusogenicity of BA.2 S and B.1.1 S was comparable in 293-ACE2/TMPRSS2  
232 cells (**Fig. 3f**). These results suggest that the relatively higher fusogenicity of  
233 BA.2 is dependent on TMPRSS2 expression on the surface of target cells. To  
234 further assess whether the TMPRSS2-dependent infection enhancement was  
235 also observed in cell-free virus, we inoculated pseudoviruses into 293-ACE2  
236 cells and 293-ACE2/TMPRSS2 cells. Although the infectivity of B.1.1 and Delta  
237 was 15.3-fold and 24.6-fold increased by TMPRSS2 expression, respectively,  
238 the TMPRSS2 expression on the target cells did not affect the infectivity of both  
239 BA.1 and BA.2 (**Fig. 3g**). These results suggest that TMPRSS2 does not affect  
240 the infectivity of cell-free BA.2 virus. However, although the growth of BA.2 and  
241 BA.1 was comparable in 293-ACE2 cells, BA.2 was more replicative than BA.1  
242 in 293-ACE2/TMPRSS2 cells (**Fig. 3h**). Overall, our data suggest that BA.2 is  
243 more fusogenic and replicative than BA.1 in a TMPRSS2-dependent fashion.

244

#### 245 **Virological features of BA.2 in vivo**

246 To investigate the dynamics of viral replication of BA.2 *in vivo*, we conducted  
247 hamster infection experiments. Consistent with our recent study<sup>12</sup>, B.1.1-infected  
248 hamsters exhibited decreased body weight and respiratory disorders that are  
249 reflected by two surrogate markers for bronchoconstriction or airway obstruction,  
250 enhanced pause (Penh) and the ratio of time to peak expiratory flow relative to  
251 the total expiratory time (Rpef), and subcutaneous oxygen saturation (SpO<sub>2</sub>),  
252 whereas BA.1-infected hamsters exhibited no or weak disorders (**Fig. 4a**).  
253 Notably, all parameters routinely measured, including body weight, Penh, Rpef  
254 and SpO<sub>2</sub>, of BA.2-infected hamsters were significantly different from uninfected  
255 and BA.1-infected hamsters, and these values were comparable to those of  
256 B.1.1-infected hamsters (**Fig. 4a**). These data suggest that BA.2 is more  
257 pathogenic than BA.1.

258 To analyse viral spread in the respiratory organs of infected hamsters,  
259 viral RNA load and nucleocapside (N) expression were assessed by RT-qPCR  
260 of viral RNA and immunohistochemistry (IHC), respectively. As shown in **Fig. 4b**,



261 viral RNA loads in the two lung regions, hilum and periphery, of BA.2-infected  
262 hamsters were significantly higher than those of BA.1-infected hamsters. In the  
263 lung periphery, the viral RNA load of BA.2 was significantly higher than that of  
264 B.1.1, and the viral RNA load of BA.2 at 1 d.p.i. was 11-fold and 9.3-fold higher  
265 than those of B.1.1 and BA.1 at the same timepoint, respectively (**Fig. 4b**). To  
266 address the possibility that BA.2 more efficiently spreads than BA.1, we  
267 investigated the positivity for N protein in the trachea and lung area close to the  
268 hilum. At 1 d.p.i., N protein was detectable in the lower tracheal epithelium in all  
269 infected hamsters, and particularly, was clearly detectable in the middle part of  
270 trachea in BA.2-infected hamsters (**Extended Data Fig. 7a**). The positivity of N  
271 protein was observed in both bronchial and bronchiolar epithelium in all infected  
272 lungs (**Extended Data Fig. 7b**). Notably, alveolar positivities were observed in  
273 B.1.1- and BA.2-infected lungs but not in BA.1-infected lungs (**Extended Data**  
274 **Fig. 7b**). Morphometry showed that the percentage of N-positive cells in  
275 BA.2-infected lungs is significantly higher than that of BA.1-infected lungs and  
276 peaked at 3 d.p.i. (**Fig. 4c** and **Extended Data Fig. 7c**). On the other hand, at 3  
277 d.p.i., the percentage of N-positive cells in the bronchus/bronchioles of  
278 BA.2-infected hamsters was 5.4-fold lower than that of BA.1-infected hamsters  
279 (**Fig. 4d**). At 5 d.p.i., N protein was almost disappeared in BA.1-infected lungs,  
280 whereas alveolar staining was still detectable in B.1.1- and BA.2-infected lungs  
281 (**Fig. 4c** and **Extended Data Fig. 7c**). These data suggest that BA.2 is more  
282 rapidly and efficiently spread in the lung tissues than BA.1.

283

### 284 **Pathogenicity of BA.2**

285 To investigate the pathogenicity of BA.2, the right lungs of infected hamsters  
286 were collected at 1, 3, and 5 d.p.i. and used them for haematoxylin and eosin  
287 (H&E) staining and histopathological analysis<sup>12,23</sup>. All histopathological  
288 parameters including bronchitis/bronchiolitis, haemorrhage, alveolar damage,  
289 and the levels of type II pneumocytes, of BA.2-infected hamsters were  
290 significantly higher than those in BA.1 (**Fig 4e** and **Extended Data Fig. 8a**). The  
291 score indicating haemorrhage including congestive edema of BA.2 was  
292 significantly higher than that of B.1.1 (**Fig. 4e**). As shown in our previous  
293 studies<sup>12,23</sup>, hyperplastic large type II pneumocytes suggesting the severity of  
294 inflammation were observed in all infected hamsters at 5 d.p.i., and particularly,  
295 the area of large type II pneumocytes in BA.2-infected hamsters was  
296 significantly larger than those in B.1.1- and BA.1-infected hamsters (**Fig. 4e**).  
297 Total histology score of BA.2 was significantly higher than that of BA.1 (**Fig. 4e**).  
298 Furthermore, in the BA.2- and B.1.1-infected lungs, the inflammation with type II  
299 alveolar pneumocyte hyperplasia was found in each lobe especially  
300 frontal/upper and accessory lobes (**Extended Data Fig. 8b**).

## 301 **Discussion**

302 Although BA.2 is considered as an Omicron variant, its genomic sequence is  
303 heavily different from BA.1, which suggests that the virological characteristics of  
304 BA.2 is different from that of BA.1. Here, we elucidated the virological  
305 characteristics of BA.2, such as its higher effective reproduction number, higher  
306 fusogenicity, higher pathogenicity when compared to BA.1. Moreover, we  
307 demonstrated that BA.2 is resistant to the BA.1-induced humoral immunity. Our  
308 data indicate that BA.2 is virologically different from BA.1 and raise a proposal  
309 that BA.2 should be given a letter of the Greek alphabet and be distinguished  
310 from BA.1, a commonly recognized Omicron variant.

311 We showed evidence suggesting that BA.2 is virologically different and  
312 distinguishable from BA.1. First, by using the two different types of antisera that  
313 were obtained from experimental animals, convalescent hamsters infected with  
314 BA.1 and mice immunized with the BA.1 S protein, we showed that the  
315 resistance of BA.2 to the BA.1-induced humoral immunity. Our results indicate  
316 that the antigenicity of BA.2 is different from BA.1. Although similar tendency  
317 was observed in human samples as well, a statistically significant difference was  
318 not observed probably because a relatively lower number of vaccine-naïve  
319 individuals who were infected with BA.1 (3 unvaccinated donors and a 1-dose  
320 vaccinated donor) were tested in the present study. The effect of BA.1-induced  
321 humoral immunity against BA.2 in humans should deeply be verified in the future  
322 investigation.

323 Second, the higher fusogenicity of BA.2 S is a pronounced  
324 characteristics in in vitro experiments. We have demonstrated that Delta S is  
325 highly fusogenic than BA.1 S and B.1.1 S, and we considered that the higher  
326 fusogenicity is attributed to the higher efficacy of S cleavage<sup>11,12,23,27</sup>. However,  
327 BA.2 S exhibited higher fusogenicity than BA.1 S without the increase of S  
328 cleavage efficacy. In recent studies<sup>12,23</sup>, we have proposed that the fusogenicity  
329 of SARS-CoV-2 variant is closely related to its pathogenicity. This hypothesis is  
330 further supported by the observations in BA.2 in the present study. However,  
331 unlike Delta, the higher fusogenicity of BA.2 appears to be not attributed to the  
332 higher efficacy of S cleavage<sup>11,12,23,27</sup>. Moreover, although TMPRSS2 increased  
333 the efficacies of both cell-cell fusion<sup>23</sup> and cell-free infection mediated by B.1.1 S  
334 and Delta S, TMPRSS2 increased the efficacy of BA.2 S-mediated cell-cell  
335 fusion but did not affect that of BA.2 S-mediated cell-free infection. These  
336 observations suggest that TMPRSS2 contributes to the cell-cell fusion and  
337 cell-free infection mediated by BA.2 S with different mechanisms of action.

338 Third, it would be most critical for global health that BA.2 exhibits higher  
339 pathogenicity than BA.1. Although clinical researches on the BA.2 pathogenicity  
340 are needed, our investigations using a hamster model showed that the  
341 pathogenicity of BA.2 is similar to that of an ancestral B.1.1 and higher than that

342 of BA.1. More importantly, the viral RNA load in the lung periphery and  
343 histopathological disorders of BA.2 were more severe than those of BA.1 and  
344 even B.1.1. Together with a higher effective reproduction number and  
345 pronounced immune resistance of BA.2, it is evident that the spread of BA.2 can  
346 be a serious issue for global health in the near future.

347 In summary, our data suggest the possibility that BA.2 would be the  
348 most concerned variant to global health. Currently, both BA.2 and BA.1 are  
349 recognised together as Omicron and these are almost undistinguishable. Based  
350 on our findings, we propose that BA.2 should be recognised as a unique variant  
351 of concern, and this SARS-CoV-2 variant should be monitored in depth.

352 **Methods**

353

354 **Ethics statement**

355 All experiments with hamsters were performed in accordance with the Science  
356 Council of Japan's Guidelines for the Proper Conduct of Animal Experiments.  
357 The protocols were approved by the Institutional Animal Care and Use  
358 Committee of National University Corporation Hokkaido University (approval ID:  
359 20-0123 and 20-0060). All experiments with mice were also performed in  
360 accordance with the Science Council of Japan's Guidelines for the Proper  
361 Conduct of Animal Experiments. The protocols were approved by the  
362 Institutional Animal Experiment Committee of The Institute of Medical Science,  
363 The University of Tokyo (approval ID: PA21-39). All protocols involving  
364 specimens from human subjects recruited at Kyoto University, Kuramochi Clinic  
365 Interpark and Chiba University were reviewed and approved by the Institutional  
366 Review Boards of Kyoto University (approval ID: G1309), Kuramochi Clinic  
367 Interpark (approval ID: G2021-004) and Chiba University (approval ID:  
368 HS202103-03). All human subjects provided written informed consent. All  
369 protocols for the use of human specimens were reviewed and approved by the  
370 Institutional Review Boards of The Institute of Medical Science, The University of  
371 Tokyo (approval IDs: 2021-1-0416 and 2021-18-0617), Kyoto University  
372 (approval ID: G0697), Kumamoto University (approval IDs: 2066 and 2074), and  
373 University of Miyazaki (approval ID: O-1021).

374

375 **Human sera collection**

376 Vaccine sera were collected from sixteen vaccinees four weeks after the second  
377 vaccination with mRNA-1273 (Moderna) (average age: 27, range: 20-47, 38%  
378 male). The sera obtained from nine vaccinees 10-25 d after the second  
379 vaccination with ChAdOx1 (Oxford-AstraZeneca) (average age: 45, range:  
380 35-54, 67% male) were purchased from BioIVT. The detail of vaccine sera is  
381 summarized in **Supplementary Table 1**.

382 Convalescent sera were collected from vaccine-naive individuals who  
383 had infected with Alpha variant (n=8; average age: 41, range: 21-57, 63% male)  
384 and Delta variant (n=15; average age: 51, range: 22-67, 80% male).  
385 Convalescent sera of BA.1-infected individuals (n=17; average age: 39, range:  
386 20-65, 47% male, 76% received the second vaccination) were also collected. To  
387 determine the SARS-CoV-2 variants infected, salivas were collected from  
388 COVID-19 patients during onset and RNA was extracted using a QIAamp viral  
389 RNA mini kit (Qiagen, Cat# 52906) according to the manufacturer's protocol. To  
390 determine Alpha and Delta variants, viral genome sequencing was performed as  
391 previously described<sup>11</sup>. For the detail, see "Viral genome sequencing" section  
392 below. To determine the BA.1 variant, mutation-targeting RT-qPCR was

393 performed. To detect the S E484A substitution (common in all Omicron variants  
394 including BA.1 and BA.2), a set of primer/probe E484A (SARS-CoV-2) (Takara,  
395 Cat# RC322A) was used. To detect the S R214EPE insertion (specific for  
396 B.1.1.529 and BA.1, undetectable in BA.2), a hand-made protocol was used with  
397 the following primers and probe: Omi\_ins214s-F1, TTC TAA GCA CAC GCC  
398 TAT TAT AGT GC; Omi\_ins214s-R1, TAA AGC CGA AAA ACC CTG AGG; and  
399 Omi\_ins214s, FAM-TGA GCC AGA AGA TC-MGB. The twelve convalescent  
400 sera during early pandemic (until May 2020) (average age: 71, range: 52-92, 8%  
401 male) were purchased from RayBiotech. Sera were inactivated at 56°C for 30  
402 min and stored at -80°C until use. The detail of convalescent sera is  
403 summarized in **Supplementary Table 2**.

404

#### 405 **Viral genome sequencing**

406 Viral genome sequencing was performed as previously described<sup>11,12,22,23</sup> with  
407 some modifications. Briefly, the sequences of the working viruses were verified  
408 by viral RNA-sequencing analysis. Viral RNA was extracted using QIAamp viral  
409 RNA mini kit (Qiagen, Cat# 52906). The sequencing library for total  
410 RNA-sequencing was prepared using NEB Next Ultra RNA Library Prep Kit for  
411 Illumina (New England Biolabs, Cat# E7530). Paired-end, 76-bp sequencing  
412 was performed using MiSeq (Illumina) with MiSeq reagent kit v3 (Illumina, Cat#  
413 MS-102-3001). Sequencing reads were trimmed using fastp v0.21.0<sup>28</sup> and  
414 subsequently mapped to the viral genome sequences of a lineage A isolate  
415 (strain WK-521; GISAID ID: EPI\_ISL\_408667)<sup>29</sup> using BWA-MEM v0.7.17<sup>30</sup>.  
416 Variant calling, filtering, and annotation were performed using SAMtools v1.9<sup>31</sup>  
417 and snpEff v5.0e<sup>32</sup>.

418

#### 419 **Phylogenetic and comparative genome analyses**

420 To construct a maximum likelihood tree of the Omicron lineages (BA.1, BA.1.1,  
421 BA.2, and BA.3) sampled from South Africa, the genome sequence data of  
422 SARS-CoV-2 and its metadata were downloaded from the GISAID database  
423 (<https://www.gisaid.org/>) on January 26, 2022. We excluded the data of viral  
424 strains with the following features from the analysis: i) lacking the collection date  
425 information; ii) sampled from animals other than humans; iii) having the flag of  
426 low coverage sequencing; or iv) having >2% of undetermined nucleotide  
427 characters. All the BA.2 and BA.3 sequences and 200 randomly sampled BA.1  
428 (including 20 BA.1.1) sequences were used for the tree construction in addition  
429 to an outgroup sequence, EPI\_ISL\_466615, the oldest isolate of B.1.1 in the UK.  
430 The viral genome sequences were mapped to the reference sequence of  
431 Wuhan-Hu-1 (GenBank accession no.: NC\_045512.2) using minimap2 v2.17<sup>33</sup>  
432 and subsequently converted to the multiple sequence alignment according to the  
433 GISAID phylogenetic analysis pipeline

434 (<https://github.com/roblanf/sarscov2phylo>). The alignment sites corresponding to  
435 the 1–265 and 29674–29903 positions in the reference genome were masked  
436 (i.e., converted to NNN). The alignment sites with >50% sequences having a  
437 gap or undetermined/ambiguous nucleotide were trimmed using trimAl v1.2<sup>34</sup>.  
438 The phylogenetic tree construction was performed by a two-step protocol: i) The  
439 first tree was constructed; ii) tips with a longer external branch (Z score > 4) were  
440 removed from the dataset; iii) and the final tree was constructed. The tree  
441 reconstruction was performed by RAxML v8.2.12<sup>35</sup> under the GTRCAT  
442 substitution model. Node support value was calculated by 100-times of bootstrap  
443 analysis.

444 We performed phylodynamics analysis of Omicron lineages (BA.1,  
445 BA.1.1, BA.2 and BA.3) sampled from South Africa as below. The SARS-CoV-2  
446 genome sequence dataset used above was split into each Omicron lineage. As  
447 an outgroup sequence, the oldest BA.2 (GISAID ID: EPI\_ISL\_8128463) was  
448 added to the BA.1 and BA.3 datasets, and the oldest BA.3 (GISAID ID:  
449 EPI\_ISL\_8616600) was added to the BA.2 dataset. The multiple sequence  
450 alignment was constructed as the procedures described above. A  
451 time-calibrated tree of each lineage was constructed by BEAST2 v.2.6.6<sup>36</sup>. The  
452 HKY model<sup>37</sup> with the four categories of discrete gamma rate variation was  
453 selected as a nucleotide substitution model. A relaxed molecular clock modelled  
454 by a log-normal distribution was selected. The exponential growth coalescent  
455 model was used. For BA.1, BA.2, and BA.3 datasets, nineteen, four, and three  
456 independent chains of Markov chain Monte Carlo (MCMC) were respectively run  
457 with 2,000,000 warmup and 18,000,000 sampling iterations. We confirmed that  
458 the effective sampling sizes for all parameters were greater than 200, indicating  
459 the MCMC runs were successfully convergent. The maximum credible trees with  
460 common ancestor heights are shown in **Extended Data Fig. 1**.

461 The number of amino acid differences (including nonsynonymous  
462 substitutions, insertions, and deletions) between SARS-CoV-2 lineages was  
463 defined as below. Information on amino acid differences of each viral strain  
464 compared with the reference sequence of Wuhan-Hu-1 (GenBank accession  
465 no.: NC\_045512.2) was extracted from the GISAID metadata (downloaded on  
466 January 26, 2022). In each viral lineage, the amino acid differences that were  
467 present in >10% sequences were extracted and subsequently counted. For the  
468 comparison of BA.1 and BA.2, the set of the symmetric difference of the amino  
469 acid differences compared with the reference was determined and subsequently  
470 counted.

471

## 472 **Modelling the epidemic dynamics of SARS-CoV-2 lineages**

473 To quantify the spread speed of each SARS-CoV-2 lineage in the human  
474 population, we estimated the relative effective reproduction number of each viral

475 lineage according to the epidemic dynamics calculated on the basis of viral  
476 genomic surveillance data. The data were downloaded from the GISAID  
477 database (<https://www.gisaid.org/>) on February 1, 2022. We excluded the data  
478 of viral strains with the following features from the analysis: i) lacking the  
479 collection date information; ii) sampled from animals other than humans; or iii)  
480 sampled by quarantine. We analysed the datasets of the eleven countries with  
481 >100 BA.2 sequences (Austria, Denmark, Germany, India, Israel, Philippines,  
482 Singapore, South Africa, Sweden, the UK, and the USA) (**Fig. 1 and Extended**  
483 **Data Fig. 2**). The dynamics of BA.1, BA.1.1, BA.2, and Delta (B.1.617.2 and AY  
484 lineages) in each country from October 1, 2021, to January 25, 2022, were  
485 analysed. The number of viral sequences of each viral lineage collected on each  
486 day in each country was counted. Finally, we constructed the L (lineage) × C  
487 (country) × T (time) = 4 × 11 × 117 shaped array, which comprises the count of  
488 each viral lineage in each country in each day. This array was used as input data  
489 for the statistical model described below.

490 We constructed a Bayesian hierarchical model to represent the relative  
491 lineage growth dynamics with a multinomial logistic regression. The  
492 mathematical theory underlying the model is described in detail elsewhere<sup>38,39</sup>,  
493 and this model is basically similar to the one used in our previous study<sup>12</sup>. In the  
494 present study, we incorporated a hierarchical structure into the slope parameter  
495 over time, which enable us to estimate the global average of the relative  
496 effective reproduction number of each viral lineage as well as that in each  
497 country. Arrays in the model index over one or more indices: L = 4 viral lineages  
498  $l$ ; C = 11 countries  $c$ ; and T = 117 days  $t$ . The model is:

$$\begin{aligned}\beta_{lc} &\sim \text{Student\_t}(6, \beta_l, \sigma_l) \\ \mu_{lct} &= \alpha_{lc} + \beta_{lc}t \\ \theta_{.ct} &= \text{softmax}(\mu_{.ct}) \\ y_{lct} &\sim \text{Multinomial}\left(\sum_l y_{lct}, \theta_{.ct}\right)\end{aligned}$$

499 The explanatory variable is time  $t$ , and the outcome variable is  $y_{lct}$ , which  
500 represents the count of viral lineage  $l$  in country  $c$  at time  $t$ . The slope  
501 parameter of lineage  $l$  in country  $c$ ,  $\beta_{lc}$ , is generated from a student's t  
502 distribution with the hyper parameters of the mean  $\beta_l$  and the standard  
503 deviation  $\sigma_l$ . As the distribution generating  $\beta_{lc}$ , we used a student's t distribution  
504 with six degrees of freedom instead of a normal distribution to reduce the effects  
505 of outlier values of  $\beta_{lc}$ . In the model, the linear estimator  $\mu_{.ct}$ , consisting of the  
506 intercept  $\alpha_{.c}$  and the slope  $\beta_{.c}$ , is converted to the simplex  $\theta_{.ct}$ , which  
507 represents the probability of occurrence of each viral lineage at time  $t$  in  
508 country  $c$ , by the softmax link function defined as:

$$\text{softmax}(x) = \frac{\exp(x)}{\sum_i \exp(x_i)}$$

509  $y_{lct}$  is generated from  $\theta_{ct}$  and the total count of all lineages at  $t$  in country  $c$   
510 according to a multinomial distribution.

511 The relative effective reproduction number of each viral lineage in each  
512 county ( $r_{lc}$ ) was calculated according to the slope parameter  $\beta_{lc}$  as:

$$r_{lc} = \exp(\gamma\beta_{lc})$$

513 where  $\gamma$  is the average viral generation time (2.1 day)  
514 ([http://sonorouschocolate.com/covid19/index.php?title=Estimating\\_Generation\\_](http://sonorouschocolate.com/covid19/index.php?title=Estimating_Generation_Time_Of_Omicron)  
515 [Time\\_Of\\_Omicron](http://sonorouschocolate.com/covid19/index.php?title=Estimating_Generation_Time_Of_Omicron)). Similarly, the global average of the relative effective  
516 reproduction number of each viral lineage was calculated according to the slope  
517 hyper parameter  $\beta_l$  as:

$$r_l = \exp(\gamma\beta_l)$$

518 For the parameter estimation, the intercept and slope parameters of the BA.1  
519 variant were fixed at 0. Consequently, the relative effective reproduction number  
520 of BA.1 was fixed at 1, and those of the respective lineages were estimated  
521 relative to that of BA.1.

522 Parameter estimation was performed by MCMC implemented in  
523 CmdStan v2.28.1 (<https://mc-stan.org>) with cmdstanr v0.4.0  
524 (<https://mc-stan.org/cmdstanr/>). Noninformative priors were set for all  
525 parameters. Four independent MCMC chains were run with 1,000 and 2,000  
526 steps in the warmup and sampling iterations, respectively. We confirmed that all  
527 estimated parameters had  $<1.01$  R-hat convergence diagnostic and  $>200$   
528 effective sampling size values, indicating that the MCMC runs were successfully  
529 convergent. The fitted model closely recapitulated the observed viral lineage  
530 dynamics in each country (**Extended Data Fig. 2c**). The analyses above were  
531 performed in R v4.1.2 (<https://www.r-project.org/>).

532

### 533 **Cell culture**

534 HEK293 cells (a human embryonic kidney cell line; ATCC CRL-1573) and  
535 HEK293-ACE2 cells [HEK293 cells (ATCC CRL-1573) stably expressing human  
536 ACE2]<sup>22</sup> were maintained in DMEM (high glucose) (Sigma-Aldrich, Cat#  
537 6429-500ML) containing 10% FBS, 1  $\mu\text{g/ml}$  puromycin (InvivoGen, Cat#  
538 ant-pr-1) and 1% PS. HEK293-ACE2/TMPRSS2 cells [HEK293 cells (ATCC  
539 CRL-1573) stably expressing human ACE2 and TMPRSS2]<sup>22</sup> were maintained  
540 in Dulbecco's modified Eagle's medium (DMEM) (high glucose) (Wako, Cat#  
541 044-29765) containing 10% foetal bovine serum (FBS) and 1%  
542 penicillin-streptomycin (PS). HEK293-C34 cells, *IFNAR1* KO HEK293 cells  
543 expressing human ACE2 and TMPRSS2 by doxycycline treatment<sup>21</sup>, were  
544 maintained in Dulbecco's modified Eagle's medium (high glucose)  
545 (Sigma-Aldrich, Cat# R8758-500ML) containing 10% FBS, 10  $\mu\text{g/ml}$  blasticidin



546 (InvivoGen, Cat# ant-bl-1) and 1% PS. Vero cells [an African green monkey  
547 (*Chlorocebus sabaeus*) kidney cell line; JCRB01111] were maintained in Eagle's  
548 minimum essential medium (EMEM) (Wako, Cat# 051-07615) containing 10%  
549 FBS and 1% PS. VeroE6/TMPRSS2 cells (VeroE6 cells stably expressing  
550 human TMPRSS2; JCRB1819)<sup>29</sup> were maintained in DMEM (low glucose)  
551 (Wako, Cat# 041-29775) containing 10% FBS, G418 (1 mg/ml; Nacalai Tesque,  
552 Cat# G8168-10ML) and 1% PS. Calu-3 cells (a human lung epithelial cell line;  
553 ATCC HTB-55) were maintained in EMEM (Sigma-Aldrich, Cat# M4655-500ML)  
554 containing 20% FBS and 1% PS. Calu-3/DSP<sub>1-7</sub> cells [Calu-3 cells (ATCC  
555 HTB-55) stably expressing DSP<sub>1-7</sub>]<sup>40</sup> were maintained in EMEM (Wako, Cat#  
556 056-08385) supplemented with 20% FBS and 1% PS. B16F10 cells (a mouse  
557 melanoma cell line; RCB2630) were maintained in DMEM (high glucose)  
558 (Sigma-Aldrich, Cat# D6429-500ML) containing 10% FBS and 1% PS. Expi293  
559 cells (Thermo Fisher Scientific, Cat# A14527) were maintained in Expi293  
560 expression medium (Thermo Fisher Scientific, Cat# A1435101). Primary human  
561 nasal epithelial cells (Cat# EP02, Batch# MP0010) were purchased from  
562 Epithelix and maintained according to the manufacturer's procedure.

563

#### 564 **Plasmid construction**

565 Plasmids expressing the SARS-CoV-2 S proteins of B.1.1 (the parental  
566 D614G-bearing variant), Alpha (B.1.1.7), Delta (B.1.617.2) and BA.1 variants  
567 were prepared in our previous studies<sup>11,12,22,23,41</sup>. Plasmids expressing the  
568 codon-optimised S proteins of BA.2 and a BA.2 derivative that loses its  
569 cytoplasmic tail were generated by site-directed overlap extension PCR using  
570 the primers listed in **Supplementary Table 3**. The resulting PCR fragment was  
571 digested with KpnI and NotI and inserted into the corresponding site of the  
572 pCAGGS vector. To construct the plasmids expressing anti-SARS-CoV-2  
573 monoclonal antibodies (Casirivimab, Imdevimab or Sotrovimab), the sequences  
574 of the variable regions of these antibodies were obtained from KEGG Drug  
575 Database (<https://www.genome.jp/kegg/drug/>) and were artificially synthesized  
576 (Fasmac). The obtained coding sequences of the variable regions of the heavy  
577 and light chains were cloned into the pCAGGS vector containing the sequences  
578 of the human immunoglobulin 1 and kappa constant region [kindly provided by  
579 Dr. Hisashi Arase (Osaka University, Japan)]. Nucleotide sequences were  
580 determined by DNA sequencing services (Eurofins), and the sequence data  
581 were analyzed by Sequencher v5.1 software (Gene Codes Corporation).

582

#### 583 **Preparation of monoclonal antibodies**

584 Casirivimab, Imdevimab and Sotrovimab were prepared as previously  
585 described<sup>11,42</sup>. Briefly, the pCAGGS vectors containing the sequences encoding  
586 the immunoglobulin heavy and light chains were cotransfected into HEK293T

587 cells using PEI Max (Polysciences, Cat# 24765-1). At 48 h posttransfection, the  
588 cell culture supernatants were harvested, and the antibodies were purified using  
589 NAb protein A plus spin kit (Thermo Fisher Scientific, Cat# 89948) according to  
590 the manufacturer's protocol.

591

### 592 **Preparation of mouse sera**

593 The SARS-CoV-2 S-immunised mouse sera were prepared as previously  
594 described<sup>42</sup>. To prepare the immunogen, B16F10 cells (2,500,000 cells) were  
595 transfected with 5 µg S expression plasmid by PEI Max (Polysciences, Cat#  
596 24765-1) according to the manufacturer's protocol. Two days posttransfection,  
597 the transfected cells were washed twice with PBS, and then the cell pellets were  
598 stored at -80°C (10,000,000 cells per stock). The expression of transfected S  
599 protein was verified by flow cytometry and western blot. BALB/c mice (female, 7  
600 weeks old) were purchased from Japan SLC Inc. (Shizuoka, Japan). The mice  
601 were maintained under specific pathogen-free conditions. For the immunisation,  
602 mice were subcutaneously immunized with the freeze-thawed S-expressing  
603 B16F10 cells in complete Freund's adjuvant (50%) (Sigma-Aldrich, Cat# F5881).  
604 Three weeks after immunisation, blood was collected in BD Microtainer blood  
605 collection tubes (BD Biosciences, Cat# 365967) and sera were collected by  
606 centrifugation.

607

### 608 **Neutralisation assay**

609 Pseudoviruses were prepared as previously described<sup>11,23,24,41,43</sup>. Briefly,  
610 lentivirus (HIV-1)-based, luciferase-expressing reporter viruses were  
611 pseudotyped with the SARS-CoV-2 spikes. HEK293T cells (1,000,000 cells)  
612 were cotransfected with 1 µg psPAX2-IN/HiBiT<sup>44</sup>, 1 µg pWPI-Luc2<sup>44</sup>, and 500 ng  
613 plasmids expressing parental S or its derivatives using PEI Max (Polysciences,  
614 Cat# 24765-1) according to the manufacturer's protocol. Two days  
615 posttransfection, the culture supernatants were harvested and centrifuged. The  
616 pseudoviruses were stored at -80°C until use.

617 For the neutralisation assay, the SARS-CoV-2 S pseudoviruses  
618 (counting ~20,000 relative light units) were incubated with serially diluted  
619 (40-fold to 29,160-fold dilution at the final concentration) heat-inactivated sera or  
620 monoclonal antibodies (Casirivimab, Imdevimab or Sotrovimab) at 37°C for 1 h.  
621 Pseudoviruses without sera were included as controls. Then, an 80 µl mixture of  
622 pseudovirus and serum/antibody was added to HOS-ACE2/TMPRSS2 cells  
623 (10,000 cells/50 µl) in a 96-well white plate. At 2 d.p.i., the infected cells were  
624 lysed with a One-Glo luciferase assay system (Promega, Cat# E6130) or a  
625 Bright-Glo™ Luciferase Assay System (Promega, Cat# E2650), and the  
626 luminescent signal was measured using a GloMax explorer multimode

627 microplate reader 3500 (Promega) or CentroXS3 (Berthold Technologies). The  
628 assay of each serum was performed in triplicate, and the 50% neutralisation titre  
629 (NT50) was calculated using Prism 9 (GraphPad Software).

630

### 631 **SARS-CoV-2 reverse genetics**

632 Recombinant SARS-CoV-2 was generated by circular polymerase extension  
633 reaction (CPER) as previously described<sup>21-23</sup>. In brief, 9 DNA fragments  
634 encoding the partial genome of SARS-CoV-2 (strain WK-521, PANGO lineage  
635 A; GISAID ID: EPI\_ISL\_408667)<sup>29</sup> were prepared by PCR using PrimeSTAR  
636 GXL DNA polymerase (Takara, Cat# R050A). A linker fragment encoding  
637 hepatitis delta virus ribozyme, bovine growth hormone poly A signal and  
638 cytomegalovirus promoter was also prepared by PCR. The corresponding  
639 SARS-CoV-2 genomic region and the PCR templates and primers used for this  
640 procedure are summarised in **Supplementary Table 4**. The 10 obtained DNA  
641 fragments were mixed and used for CPER<sup>21</sup>. To prepare GFP-expressing  
642 replication-competent recombinant SARS-CoV-2, we used fragment 9, in which  
643 the *GFP* gene was inserted in the *ORF7a* frame, instead of the authentic F9  
644 fragment (see **Extended Data Fig. 4** and **Supplementary Table 4**)<sup>21</sup>.

645 To produce recombinant SARS-CoV-2, the CPER products were  
646 transfected into HEK293-C34 cells using TransIT-LT1 (Takara, Cat# MIR2300)  
647 according to the manufacturer's protocol. At one day posttransfection, the  
648 culture medium was replaced with Dulbecco's modified Eagle's medium (high  
649 glucose) (Sigma-Aldrich, Cat# R8758-500ML) containing 2% FCS, 1% PS and  
650 doxycycline (1 µg/ml; Takara, Cat# 1311N). At six days posttransfection, the  
651 culture medium was harvested and centrifuged, and the supernatants were  
652 collected as the seed virus. To remove the CPER products (i.e.,  
653 SARS-CoV-2-related DNA), 1 ml of the seed virus was treated with 2 µl TURBO  
654 DNase (Thermo Fisher Scientific, Cat# AM2238) and incubated at 37°C for 1 h.  
655 Complete removal of the CPER products (i.e., SARS-CoV-2-related DNA) from  
656 the seed virus was verified by PCR. The working virus stock was prepared from  
657 the seed virus as described above.

658 To generate chimeric recombinant SARS-CoV-2 that encodes the S  
659 proteins of B.1.1, BA.1 and BA.2 (**Extended Data Fig. 4**), mutations were  
660 inserted in fragment 8 (**Supplementary Table 4**) using the GENEART  
661 site-directed mutagenesis system (Thermo Fisher Scientific, Cat# A13312)  
662 according to the manufacturer's protocol with the primers listed in  
663 **Supplementary Table 5**. A recombinant SARS-CoV-2 that bears D614G S  
664 (corresponds to B.1.1 S) was prepared in our previous study<sup>23</sup>. To prepare a  
665 chimeric recombinant SARS-CoV-2 that bears Delta S (**Extended Data Fig. 4**),  
666 the fragment of viral genome that corresponds to the region of fragment 8  
667 (**Supplementary Table 4**) was subcloned from a Delta isolate (strain

668 TKYTK1734; GISAID ID: EPI\_ISL\_2378732)<sup>23</sup>. Nucleotide sequences were  
669 determined by a DNA sequencing service (Fasmac), and the sequence data  
670 were analysed by Sequencher software v5.1 (Gene Codes Corporation).

671 To produce chimeric recombinant SARS-CoV-2, the CPER products  
672 were transfected into HEK293-C34 cells using TransIT-LT1 (Takara, Cat#  
673 MIR2300) according to the manufacturer's protocol. At 1 day posttransfection,  
674 the culture medium was replaced with Dulbecco's modified Eagle's medium  
675 (high glucose) (Sigma-Aldrich, Cat# R8758-500ML) containing 2% FCS, 1% PS  
676 and doxycycline (1 µg/ml; Takara, Cat# 1311N). At 7 days posttransfection, the  
677 culture medium was harvested and centrifuged, and the supernatants were  
678 collected as the seed virus. To remove the CPER products (i.e.,  
679 SARS-CoV-2-related DNA), 1 ml of the seed virus was treated with 2 µl TURBO  
680 DNase (Thermo Fisher Scientific, Cat# AM2238) and incubated at 37°C for 1 h.  
681 Complete removal of the CPER products (i.e., SARS-CoV-2-related DNA) from  
682 the seed virus was verified by PCR. The working virus stock was prepared from  
683 the seed virus as described below (see "SARS-CoV-2 preparation and titration"  
684 section).

685

#### 686 **SARS-CoV-2 preparation and titration**

687 The working virus stocks of chimeric recombinant SARS-CoV-2 that encodes the  
688 S proteins of B.1.1, Delta, BA.1 and BA.2 were prepared and titrated as  
689 previously described<sup>21-23</sup>. In brief, 20 µl of the seed virus was inoculated into  
690 VeroE6/TMPRSS2 cells (5,000,000 cells in a T-75 flask). One hour after  
691 infection (h.p.i.), the culture medium was replaced with DMEM (low glucose)  
692 (Wako, Cat# 041-29775) containing 2% FBS and 1% PS. At 3 d.p.i., the culture  
693 medium was harvested and centrifuged, and the supernatants were collected as  
694 the working virus stock.

695 The titre of the prepared working virus was measured as the 50%  
696 tissue culture infectious dose (TCID<sub>50</sub>). Briefly, one day before infection,  
697 VeroE6/TMPRSS2 cells (10,000 cells) were seeded into a 96-well plate. Serially  
698 diluted virus stocks were inoculated into the cells and incubated at 37°C for 4 d.  
699 The cells were observed under microscopy to judge the CPE appearance. The  
700 value of TCID<sub>50</sub>/ml was calculated with the Reed–Muench method<sup>45</sup>.

701 To verify the sequence of chimeric recombinant SARS-CoV-2, viral  
702 RNA was extracted from the working viruses using a QIAamp viral RNA mini kit  
703 (Qiagen, Cat# 52906) and viral genome sequence was analysed as described  
704 above (see "Viral genome sequencing" section). In brief, the viral sequences of  
705 GFP-encoding recombinant SARS-CoV-2 (strain WK-521; GISAID ID:  
706 EPI\_ISL\_408667)<sup>21,29</sup> that harbour the S genes of respective variants (B.1.1,  
707 BA.1 or BA.2) were used for the reference. Information on the unexpected

708 mutations detected is summarized in **Supplementary Table 6**, and the raw data  
709 are deposited in Gene Expression Omnibus (accession number: GSE196649).

710

### 711 **SARS-CoV-2 infection**

712 One day before infection, Vero cells (10,000 cells), VeroE6/TMPRSS2 cells  
713 (10,000 cells), Calu-3 cells (20,000 cells), HEK293-ACE2 cells (10,000 cells),  
714 HEK293-ACE2/TMPRSS2 cells (10,000 cells), were seeded into a 96-well plate.  
715 SARS-CoV-2 [100 TCID<sub>50</sub> for VeroE6/TMPRSS2 cells (**Fig. 3a**), 1,000 TCID<sub>50</sub>  
716 for Vero cells (**Fig. 3a**), HEK293-ACE2 cells (10,000 cells) (**Fig. 3j**), and  
717 HEK293-ACE2/TMPRSS2 cells (10,000 cells) (**Fig. 3j**); and 2,000 TCID<sub>50</sub> for  
718 Calu-3 cells (**Fig. 3a**)] was inoculated and incubated at 37°C for 1 h. The  
719 infected cells were washed, and 180 µl of culture medium was added. The  
720 culture supernatant (10 µl) was harvested at the indicated timepoints and used  
721 for RT-qPCR to quantify the viral RNA copy number (see “RT-qPCR” section  
722 below).

723 The infection experiment primary human nasal epithelial cells (**Fig. 3a**)  
724 was performed as previously described<sup>11,23</sup>. Briefly, the working viruses were  
725 diluted with Opti-MEM (Thermo Fisher Scientific, Cat# 11058021). The diluted  
726 viruses (1,000 TCID<sub>50</sub> in 100 µl) were inoculated onto the apical side of the  
727 culture and incubated at 37°C for 1 h. The inoculated viruses were removed and  
728 washed twice with Opti-MEM. To harvest the viruses on the apical side of the  
729 culture, 100 µl Opti-MEM was applied onto the apical side of the culture and  
730 incubated at 37°C for 10 m. The Opti-MEM applied was harvested and used for  
731 RT-qPCR to quantify the viral RNA copy number (see “RT-qPCR” section  
732 below).

733

### 734 **RT-qPCR**

735 RT-qPCR was performed as previously described<sup>11,12,22,23</sup>. Briefly, 5 µl of culture  
736 supernatant was mixed with 5 µl of 2 × RNA lysis buffer [2% Triton X-100, 50  
737 mM KCl, 100 mM Tris-HCl (pH 7.4), 40% glycerol, 0.8 U/µl recombinant RNase  
738 inhibitor (Takara, Cat# 2313B)] and incubated at room temperature for 10 min.  
739 RNase-free water (90 µl) was added, and the diluted sample (2.5 µl) was used  
740 as the template for real-time RT-PCR performed according to the manufacturer’s  
741 protocol using the One Step TB Green PrimeScript PLUS RT-PCR kit (Takara,  
742 Cat# RR096A) and the following primers: Forward *N*, 5'-AGC CTC TTC TCG  
743 TTC CTC ATC AC-3'; and Reverse *N*, 5'-CCG CCA TTG CCA GCC ATT C-3'.  
744 The viral RNA copy number was standardized with a SARS-CoV-2 direct  
745 detection RT-qPCR kit (Takara, Cat# RC300A). Fluorescent signals were  
746 acquired using QuantStudio 3 Real-Time PCR system (Thermo Fisher Scientific),  
747 CFX Connect Real-Time PCR Detection system (Bio-Rad), Eco Real-Time PCR

748 System (Illumina), qTOWER3 G Real-Time System (Analytik Jena) or 7500  
749 Real-Time PCR System (Thermo Fisher Scientific).

750

### 751 **Fluorescence microscopy**

752 Fluorescence microscopy (**Fig. 3b** and **Extended Data Fig. 5a**) was performed  
753 as previously described<sup>23</sup>. Briefly, one day before infection, VeroE6/TMPRSS2  
754 cells (10,000 cells) were seeded into 96-well, glass bottom, black plates and  
755 infected with SARS-CoV-2 (100 TCID<sub>50</sub>). At 24, 48, and 72 h.p.i., GFP  
756 fluorescence was observed under an All-in-One Fluorescence Microscope  
757 BZ-X800 (Keyence) in living cells, and a 13-square-millimeter area of each  
758 sample was scanned. Images were reconstructed using an BZ-X800 analyzer  
759 software (Keyence), and the area of the GFP-positive cells was measured using  
760 this software.

761

### 762 **Plaque assay**

763 Plaque assay (**Fig. 3c** and **Extended Data Fig. 5b**) was performed as  
764 previously described<sup>12,22,23</sup>. Briefly, one day before infection, VeroE6/TMPRSS2  
765 cells (100,000 cells) were seeded into a 24-well plate and infected with  
766 SARS-CoV-2 (1, 10, 100 and 1,000 TCID<sub>50</sub>) at 37°C for 2 h. Mounting solution  
767 containing 3% FBS and 1.5% carboxymethyl cellulose (Wako, Cat# 039-01335)  
768 was overlaid, followed by incubation at 37°C. At 3 d.p.i., the culture medium was  
769 removed, and the cells were washed with PBS three times and fixed with 4%  
770 paraformaldehyde phosphate (Nacalai Tesque, Cat# 09154-85). The fixed cells  
771 were washed with tap water, dried, and stained with staining solution [0.1%  
772 methylene blue (Nacalai Tesque, Cat# 22412-14) in water] for 30 m. The stained  
773 cells were washed with tap water and dried, and the size of plaques was  
774 measured using Fiji software v2.2.0 (ImageJ).

775

### 776 **Coculture experiment**

777 Coculture experiment (**Extended Data Fig. 5c**) was performed as previously  
778 described<sup>12</sup>. Briefly, one day before transfection, effector cells (i.e., S-expressing  
779 cells) were seeded on the poly-L-lysine (Sigma, Cat# P4832) coated coverslips  
780 put in a 12-well plate, and target cells were prepared at a density of 100,000  
781 cells in a 12-well plate. To prepare effector cells, HEK293 cells were  
782 cotransfected with the S-expression plasmids (500 ng) and pDSP<sub>8-11</sub> (500 ng)  
783 using PEI Max (Polysciences, Cat# 24765-1). To prepare target cells, HEK293  
784 and HEK293-ACE2/TMPRSS2 cells were transfected with pDSP<sub>1-7</sub> (500 ng). At  
785 24 h posttransfection, target cells were detached and cocultured with effector  
786 cells in a 1:2 ratio. At 9 h post-coculture, cells were fixed with 4%  
787 paraformaldehyde in PBS (Nacalai Tesque, Cat# 09154-85) for 15 m at room  
788 temperature. Nuclei were stained with Hoechst 33342 (Thermo Fisher Scientific,

789 Cat# H3570). The coverslips were mounted on glass slides using  
790 Fluoromount-G (Southern Biotechnology, Cat# 0100-01) with Hoechst 33342  
791 and observed using an A1Rsi Confocal Microscope (Nikon). The size of  
792 syncytium (GFP-positive area) was measured using Fiji software v2.2.0  
793 (ImageJ) as previously described<sup>12</sup>.

794

### 795 **SARS-CoV-2 S-based fusion assay**

796 SARS-CoV-2 S-based fusion assay (**Fig. 3d and 3f**) was performed as  
797 previously described<sup>12,22,23</sup>. This assay utilizes a dual split protein (DSP)  
798 encoding *Renilla* luciferase and *GFP* genes; the respective split proteins,  
799 DSP<sub>8-11</sub> and DSP<sub>1-7</sub>, are expressed in effector and target cells by transfection.  
800 Briefly, on day 1, effector cells (i.e., S-expressing cells) and target cells (see  
801 below) were prepared at a density of 0.6–0.8 × 10<sup>6</sup> cells in a 6-well plate. To  
802 prepare effector cells, HEK293 cells were cotransfected with the S expression  
803 plasmids (400 ng) and pDSP<sub>8-11</sub> (400 ng) using TransIT-LT1 (Takara, Cat#  
804 MIR2300). To prepare target cells, HEK293 cells were cotransfected with  
805 pC-ACE2 (200 ng) and pDSP<sub>1-7</sub> (400 ng). Target HEK293 cells in selected wells  
806 were cotransfected with pC-TMPRSS2 (40 ng) in addition to the plasmids above.  
807 VeroE6/TMPRSS2 cells, Calu-3 cells, HEK293-ACE2 cells and  
808 HEK293-ACE2/TMPRSS2 cells were transfected with pDSP<sub>1-7</sub> (400ng). On day  
809 3 (24 h posttransfection), 16,000 effector cells were detached and reseeded into  
810 96-well black plates (PerkinElmer, Cat# 6005225), and target cells (HEK293,  
811 VeroE6/TMPRSS2 or Calu-3/DSP<sub>1-7</sub> cells) were reseeded at a density of  
812 1,000,000 cells/2 ml/well in 6-well plates. On day 4 (48 h posttransfection), target  
813 cells were incubated with EnduRen live cell substrate (Promega, Cat# E6481)  
814 for 3 h and then detached, and 32,000 target cells were added to a 96-well plate  
815 with effector cells. *Renilla* luciferase activity was measured at the indicated time  
816 points using Centro XS3 LB960 (Berthold Technologies). To measure the  
817 surface expression level of S protein, effector cells were stained with rabbit  
818 anti-SARS-CoV-2 S S1/S2 polyclonal antibody (Thermo Fisher Scientific, Cat#  
819 PA5-112048, 1:100). Normal rabbit IgG (SouthernBiotech, Cat# 0111-01, 1:100)  
820 was used as negative controls, and APC-conjugated goat anti-rabbit IgG  
821 polyclonal antibody (Jackson ImmunoResearch, Cat# 111-136-144, 1:50) was  
822 used as a secondary antibody. Surface expression level of S proteins  
823 (**Extended Data Fig. 6a**) was measured using FACS Canto II (BD Biosciences)  
824 and the data were analysed using FlowJo software v10.7.1 (BD Biosciences).  
825 Gating strategy for flow cytometry is shown in **Supplementary Fig. 1**. To  
826 calculate fusion activity, *Renilla* luciferase activity was normalized to the MFI of  
827 surface S proteins. The normalized value (i.e., *Renilla* luciferase activity per the  
828 surface S MFI) is shown as fusion activity.

829

### 830 **Yeast surface display**

831 Yeast surface display (**Extended Data Fig. 6b**) was performed as previously  
832 described as previously described<sup>22,24,46</sup>. Briefly, the peptidase domain of human  
833 ACE2 (residues 18-740) was expressed in Expi293 cells and purified by a 5-ml  
834 HisTrap Fast Flow column (Cytiva, Cat# 17-5255-01) and Superdex 200 16/600  
835 (Cytiva, Cat# 28-9893-35) using an ÄKTA pure chromatography system (Cytiva),  
836 and the purified soluble ACE2 was labelled with CF640 (Biotium, Cat# 92108).  
837 Protein quality was verified using a Tycho NT.6 system (NanoTemper) and  
838 ACE2 activity assay kit (Sensolyte, Cat# AS-72086).

839 An enhanced yeast display platform for SARS-CoV-2 RBD [wild-type  
840 (B.1.1), residues 336-528] yeast surface expression was established using  
841 *Saccharomyces cerevisiae* EBY100 strain and pJYDC1 plasmid (Addgene, Cat#  
842 162458) as previously described<sup>22,24,47</sup>. The yeast-optimized  
843 SARS-CoV-2\_RBD-Omicron-BA.1 gene (**Supplementary Table 7**) was  
844 obtained from Twist Biosciences. The site-directed mutagenesis was performed  
845 using the KAPA HiFi HotStart ReadyMix kit (Roche, Cat# KK2601) by restriction  
846 enzyme-free cloning procedure<sup>48</sup>. Primers for mutagenesis are listed in  
847 **Supplementary Table 8**.

848 The binding affinity of SARS-CoV-2 S B.1.1, BA.1, and BA.2 RBDs to  
849 human ACE2 were titrated by flow cytometry. The CF640-labelled ACE2 at  
850 12–14 different concentrations (200 nM to 13 pM in PBS supplemented with  
851 bovine serum albumin at 1 g/l) per measurement were incubated with expressed  
852 yeast aliquots and 1 nM bilirubin (Sigma-Aldrich, Cat# 14370-1G) and analysed  
853 by using FACS S3e Cell Sorter device (Bio-Rad) as previously described<sup>22,24,47</sup>.  
854 The background binding subtracted fluorescent signal was fitted to a standard  
855 noncooperative Hill equation by nonlinear least-squares regression using Python  
856 v3.7 (<https://www.python.org>) as previously described<sup>47</sup>.

857

### 858 **TMPRSS2 expression on the cell surface**

859 To measure the surface expression level of TMPRSS2 (**Extended Data Fig. 6c**),  
860 HEK293-ACE2 cells and HEK293-ACE2/TMPRSS2 cells were stained with  
861 rabbit anti-TMPRSS2 polyclonal antibody (BIOSS, Cat# BS-6285R, 1:100).  
862 Normal rabbit IgG (SouthernBiotech, Cat# 0111-01, 1:100) was used as  
863 negative controls, and APC-conjugated goat anti-rabbit IgG polyclonal antibody  
864 (Jackson ImmunoResearch, Cat# 111-136-144, 1:50) was used as a secondary  
865 antibody. Surface expression level of TMPRSS2 was measured using FACS  
866 Canto II (BD Biosciences) and the data were analysed using FlowJo software  
867 v10.7.1 (BD Biosciences). Gating strategy for flow cytometry is shown in  
868 **Supplementary Fig. 1**.

869

### 870 **Western blot**



871 Western blot (**Fig. 3e**) was performed as previously described<sup>12,22,23</sup>. The  
872 HEK293 cells cotransfected with the S expression plasmids and pDSP<sub>8-11</sub> (see  
873 “SARS-CoV-2 S-based fusion assay” section above) were used. To quantify the  
874 level of the cleaved S2 protein in the cells, the harvested cells were washed and  
875 lysed in lysis buffer [25 mM HEPES (pH 7.2), 20% glycerol, 125 mM NaCl, 1%  
876 Nonidet P40 substitute (Nacalai Tesque, Cat# 18558-54), protease inhibitor  
877 cocktail (Nacalai Tesque, Cat# 03969-21)]. After quantification of total protein by  
878 protein assay dye (Bio-Rad, Cat# 5000006), lysates were diluted with 2 ×  
879 sample buffer [100 mM Tris-HCl (pH 6.8), 4% SDS, 12% β-mercaptoethanol,  
880 20% glycerol, 0.05% bromophenol blue] and boiled for 10 m. Then, 10 μl  
881 samples (50 μg of total protein) were subjected to Western blot. For protein  
882 detection, the following antibodies were used: mouse anti-SARS-CoV-2 S  
883 monoclonal antibody (clone 1A9, GeneTex, Cat# GTX632604, 1:10,000), rabbit  
884 anti-beta actin (ACTB) monoclonal antibody (clone 13E5, Cell Signalling, Cat#  
885 4970, 1:5,000), horseradish peroxidase (HRP)-conjugated donkey anti-rabbit  
886 IgG polyclonal antibody (Jackson ImmunoResearch, Cat# 711-035-152,  
887 1:10,000) and HRP-conjugated donkey anti-mouse IgG polyclonal antibody  
888 (Jackson ImmunoResearch, Cat# 715-035-150, 1:10,000). Chemiluminescence  
889 was detected using SuperSignal West Femto Maximum Sensitivity Substrate  
890 (Thermo Fisher Scientific, Cat# 34095) according to the manufacturer’s  
891 instruction. Bands were visualized using an Amersham Imager 600 (GE  
892 Healthcare), and the band intensity was quantified using Image Studio Lite v5.2  
893 (LI-COR Biosciences) or Fiji software v2.2.0 (ImageJ). Uncropped blots are  
894 shown in **Supplementary Fig. 2**.

895

### 896 **Pseudovirus infection**

897 Pseudovirus infection was (**Fig. 3g**) performed as previously  
898 described<sup>11,12,22-24,43</sup>. Briefly, the same amount of pseudoviruses (normalized to  
899 the HiBiT value, which indicates the amount of p24 HIV-1 antigen) was  
900 inoculated into HEK293-ACE2 cells or HEK293-ACE2/TMPRSS2 and viral  
901 infectivity was measured as described above (see “Neutralisation assay”  
902 section). To analyse the effect of TMPRSS2 for pseudovirus infectivity, the fold  
903 change of the values of HEK293-ACE2/TMPRSS2 to HEK293-ACE2 was  
904 calculated.

905

### 906 **Animal experiments**

907 Animal experiments (**Fig. 4**) were performed as previously described<sup>12,23</sup>. Syrian  
908 hamsters (male, 4 weeks old) were purchased from Japan SLC Inc. (Shizuoka,  
909 Japan). Baseline body weights were measured before infection. For the virus  
910 infection experiments, hamsters were euthanized by intramuscular injection of a  
911 mixture of either 0.15 mg/kg medetomidine hydrochloride (Domitor<sup>®</sup>, Nippon

912 Zenyaku Kogyo), 2.0 mg/kg midazolam (Dormicum<sup>®</sup>, FUJIFILM Wako  
913 Chemicals) and 2.5 mg/kg butorphanol (Vetorphale<sup>®</sup>, Meiji Seika Pharma), or  
914 0.15 mg/kg medetomidine hydrochloride, 2.0 mg/kg alphaxalone (Alfaxan<sup>®</sup>,  
915 Jurox) and 2.5 mg/kg butorphanol. The B.1.1 virus, Delta, Omicron (10,000  
916 TCID<sub>50</sub> in 100 µl), or saline (100 µl) were intranasally inoculated under  
917 anaesthesia. Oral swabs were daily collected under anaesthesia with isoflurane  
918 (Sumitomo Dainippon Pharma). Body weight, enhanced pause (Penh), the ratio  
919 of time to peak expiratory flow relative to the total expiratory time (Rpef) and  
920 subcutaneous oxygen saturation (SpO<sub>2</sub>) were routinely monitored at indicated  
921 timepoints (see “Lung function test” section below). Respiratory organs were  
922 anatomically collected at 1, 3 and 5 d.p.i (for lung) or 1 d.p.i. (for trachea). Viral  
923 RNA load in the respiratory tissues were determined by RT-qPCR. The  
924 respiratory tissues were also used for histopathological and IHC analyses (see  
925 “H&E staining” and “IHC” sections below).

926

### 927 **Lung function test**

928 Lung function test (**Fig. 4a**) was performed as previously described<sup>12</sup>.  
929 Respiratory parameters (Penh and Rpef) were measured by using a whole-body  
930 plethysmography system (DSI) according to the manufacturer's instructions. In  
931 brief, a hamster was placed in an unrestrained plethysmography chamber and  
932 allowed to acclimatize for 30 s, then, data were acquired over a 4-m period by  
933 using FinePointe Station and Review softwares v2.9.2.12849 (STARR). The  
934 state of oxygenation was examined by measuring SpO<sub>2</sub> using pulse oximeter,  
935 MouseOx PLUS (STARR). SpO<sub>2</sub> was measured by attaching a measuring chip  
936 to the neck of hamsters sedated by 0.25 mg/kg medetomidine hydrochloride.

937

### 938 **IHC**

939 IHC (**Extended Data Fig. 7**) was performed as previously described<sup>12,23</sup> using  
940 an Autostainer Link 48 (Dako). The deparaffinized sections were exposed to  
941 EnVision FLEX target retrieval solution high pH (Agilent, Cat# K8004) for 20 m at  
942 97°C to activate, and mouse anti-SARS-CoV-2 N monoclonal antibody (R&D  
943 systems, Clone 1035111, Cat# MAB10474-SP, 1:400) was used as a primary  
944 antibody. The sections were sensitized using EnVision FLEX (Agilent) for 15 m  
945 and visualised by peroxidase-based enzymatic reaction with  
946 3,3'-diaminobenzidine tetrahydrochloride as substrate for 5 m. The N protein  
947 positivity (**Fig. 4c and 4d**) was evaluated by certificated pathologists as  
948 previously described<sup>12</sup>. Images were incorporated as virtual slide by  
949 NDRscan3.2 software (Hamamatsu Photonics). The N-protein positivity was  
950 measured as the area using Fiji software v2.2.0 (ImageJ).

951

### 952 **H&E staining**

953 H&E staining (**Extended Data Fig. 8**) was performed as previously  
954 described<sup>12,23</sup>. Briefly, excised animal tissues were fixed with 10% formalin  
955 neutral buffer solution, and processed for paraffin embedding. The paraffin  
956 blocks were sectioned with 3  $\mu\text{m}$ -thickness and then mounted on silane-coated  
957 glass slides (MAS-GP, Matsunami). H&E staining was performed according to a  
958 standard protocol.

959

### 960 **Histopathological scoring**

961 Histopathological scoring (**Fig. 4e** and **Extended Data Fig. 8a**) was performed  
962 as previously described<sup>12,23</sup>. Pathological features including bronchitis or  
963 bronchiolitis, haemorrhage with congestive edema, alveolar damage with  
964 epithelial apoptosis and macrophage infiltration, hyperplasia of type II  
965 pneumocytes, and the area of the hyperplasia of large type II pneumocytes were  
966 evaluated by certified pathologists and the degree of these pathological findings  
967 were arbitrarily scored using four-tiered system as 0 (negative), 1 (weak), 2  
968 (moderate), and 3 (severe). The "large type II pneumocytes" are the hyperplasia  
969 of type II pneumocytes exhibiting more than 10- $\mu\text{m}$ -diameter nucleus. We  
970 described "large type II pneumocytes" as one of the remarkable  
971 histopathological features reacting SARS-CoV-2 infection in our previous  
972 studies<sup>12,23</sup>. Total histology score is the sum of these five indices.

973 To measure the inflammation area in the infected lungs (**Extended**  
974 **Data Fig. 8b**), four hamsters infected with each virus were sacrificed at the 1, 3  
975 and 5 d.p.i., and all four right lung lobes, including upper (anterior/cranial),  
976 middle, lower (posterior/caudal), and accessory lobes, were sectioned along  
977 with their bronchi. The tissue sections were stained by H&E, and the digital  
978 microscopic images were incorporated into virtual slides using NDRscan3.2  
979 software (Hamamatsu Photonics). The inflammatory area including type II  
980 pneumocyte hyperplasia in the infected whole lungs was morphometrically  
981 analysed using Fiji software v2.2.0 (ImageJ).

982

### 983 **Statistics and reproducibility**

984 Statistical significance was tested using a two-sided Student's *t*-test or a  
985 two-sided Mann–Whitney *U*-test unless otherwise noted. The tests above were  
986 performed using Prism 9 software v9.1.1 (GraphPad Software).

987 In the time-course experiments (**Fig. 3a, 3d, 3f, 3h, 4a–4c, and 4e**), a  
988 multiple regression analysis including experimental conditions (i.e., the types of  
989 infected viruses) as explanatory variables and timepoints as qualitative control  
990 variables was performed to evaluate the difference between experimental  
991 conditions thorough all timepoints. *P* value was calculated by a two-sided Wald  
992 test. Subsequently, familywise error rates (FWERs) were calculated by the Holm  
993 method. These analyses were performed in v4.1.2 (<https://www.r-project.org/>).

994            In **Extended Data Fig. 7 and 8**, photographs shown are the  
995 representative areas of at least two independent experiments by using four  
996 hamsters at each timepoint. In **Extended Data Fig. 5**, assays were performed in  
997 triplicate. Photographs shown are the representatives of >20 fields of view taken  
998 for each sample.

999

#### 1000 **Data availability**

1001 The raw data of virus sequences analysed in this study are deposited in Gene  
1002 Expression Omnibus (accession number: GSE196649). All databases/datasets  
1003 used in this study are available from GISAID database (<https://www.gisaid.org>)  
1004 and Genbank database (<https://www.ncbi.nlm.nih.gov/genbank/>). The accession  
1005 numbers of viral sequences used in this study are listed in Method section.

1006

#### 1007 **Code availability**

1008 The computational code to estimate the relative effective reproduction number of  
1009 each viral lineage (**Fig. 1**) is available in the GitHub repository  
1010 ([https://github.com/TheSatoLab/Omicron\\_BA2/tree/main/lineage\\_growth\\_hierar  
1011 chical\\_model](https://github.com/TheSatoLab/Omicron_BA2/tree/main/lineage_growth_hierarchical_model)).

## 1012 References

- 1013 1 WHO. "Classification of Omicron (B.1.1.529): SARS-CoV-2 variant of  
1014 concern (November 26, 2021)"  
1015 [https://www.who.int/news/item/26-11-2021-classification-of-omicron-\(b.1.  
1016 1.529\)-sars-cov-2-variant-of-concern](https://www.who.int/news/item/26-11-2021-classification-of-omicron-(b.1.1.529)-sars-cov-2-variant-of-concern). (2021).
- 1017 2 WHO. "Tracking SARS-CoV-2 variants (February 3, 2022)".  
1018 <https://www.who.int/en/activities/tracking-SARS-CoV-2-variants/>.  
1019 (2022).
- 1020 3 UKHSA. "SARS-CoV-2 variants of concern and variants under  
1021 investigation in England. Technical briefing 35 (January 28, 2022)".  
1022 [https://assets.publishing.service.gov.uk/government/uploads/system/uplo  
1023 ads/attachment\\_data/file/1050999/Technical-Briefing-35-28January2022.  
1024 pdf](https://assets.publishing.service.gov.uk/government/uploads/system/uploads/attachment_data/file/1050999/Technical-Briefing-35-28January2022.pdf). (2022).
- 1025 4 Cele, S. *et al.* Omicron extensively but incompletely escapes Pfizer  
1026 BNT162b2 neutralization. *Nature*, doi:  
1027 <https://doi.org/10.1038/d41586-41021-03824-41585> (2021).
- 1028 5 Cao, Y. *et al.* Omicron escapes the majority of existing SARS-CoV-2  
1029 neutralizing antibodies. *Nature*, doi:  
1030 <https://doi.org/10.1038/d41586-41021-03796-41586> (2021).
- 1031 6 Dejnirattisai, W. *et al.* Reduced neutralisation of SARS-CoV-2 omicron  
1032 B.1.1.529 variant by post-immunisation serum. *Lancet*,  
1033 doi:[https://doi.org/10.1016/S0140-6736\(2021\)02844-02840](https://doi.org/10.1016/S0140-6736(2021)02844-02840) (2021).
- 1034 7 Cameroni, E. *et al.* Broadly neutralizing antibodies overcome  
1035 SARS-CoV-2 Omicron antigenic shift. *Nature*, doi:  
1036 <https://doi.org/10.1038/d41586-41021-03825-41584> (2021).
- 1037 8 Garcia-Beltran, W. F. *et al.* mRNA-based COVID-19 vaccine boosters  
1038 induce neutralizing immunity against SARS-CoV-2 Omicron variant. *Cell*,  
1039 doi: <https://doi.org/10.1016/j.cell.2021.1012.1033> (2021).
- 1040 9 Planas, D. *et al.* Considerable escape of SARS-CoV-2 Omicron to  
1041 antibody neutralization. *Nature*, doi:  
1042 <https://doi.org/10.1038/d41586-41021-03827-41582> (2021).
- 1043 10 Liu, L. *et al.* Striking antibody evasion manifested by the Omicron variant  
1044 of SARS-CoV-2. *Nature*, doi:  
1045 <https://doi.org/10.1038/d41586-41021-03826-41583> (2021).
- 1046 11 Meng, B. *et al.* Altered TMPRSS2 usage by SARS-CoV-2 Omicron  
1047 impacts tropism and fusogenicity. *Nature*,  
1048 doi:10.1038/s41586-022-04474-x (2022).
- 1049 12 Suzuki, R. *et al.* Attenuated fusogenicity and pathogenicity of  
1050 SARS-CoV-2 Omicron variant. *Nature*, doi:10.1038/s41586-022-04462-1  
1051 (2022).
- 1052 13 Shuai, H. *et al.* Attenuated replication and pathogenicity of SARS-CoV-2

- 1053 B.1.1.529 Omicron. *Nature*, doi:10.1038/s41586-022-04442-5 (2022).
- 1054 14 Halfmann, P. J. *et al.* SARS-CoV-2 Omicron virus causes attenuated  
1055 disease in mice and hamsters. *Nature*, doi:10.1038/s41586-022-04441-6  
1056 (2022).
- 1057 15 Han, P. *et al.* Receptor binding and complex structures of human ACE2 to  
1058 spike RBD from omicron and delta SARS-CoV-2. *Cell*,  
1059 doi:10.1016/j.cell.2022.01.001 (2022).
- 1060 16 Dejnirattisai, W. *et al.* SARS-CoV-2 Omicron-B.1.1.529 leads to  
1061 widespread escape from neutralizing antibody responses. *Cell* **185**,  
1062 467-484 e415, doi:10.1016/j.cell.2021.12.046 (2022).
- 1063 17 Cameroni, E. *et al.* Broadly neutralizing antibodies overcome  
1064 SARS-CoV-2 Omicron antigenic shift. *Nature*,  
1065 doi:10.1038/s41586-021-04386-2 (2021).
- 1066 18 Takashita, E. *et al.* Efficacy of Antibodies and Antiviral Drugs against  
1067 Covid-19 Omicron Variant. *N Engl J Med*, doi:10.1056/NEJMc2119407  
1068 (2022).
- 1069 19 VanBlargan, L. A. *et al.* An infectious SARS-CoV-2 B.1.1.529 Omicron  
1070 virus escapes neutralization by therapeutic monoclonal antibodies. *Nat*  
1071 *Med*, doi:10.1038/s41591-021-01678-y (2022).
- 1072 20 Viana, R. *et al.* Rapid epidemic expansion of the SARS-CoV-2 Omicron  
1073 variant in southern Africa. *Nature*, doi:10.1038/s41586-022-04411-y  
1074 (2022).
- 1075 21 Torii, S. *et al.* Establishment of a reverse genetics system for  
1076 SARS-CoV-2 using circular polymerase extension reaction. *Cell Rep* **35**,  
1077 109014 (2021).
- 1078 22 Motozono, C. *et al.* SARS-CoV-2 spike L452R variant evades cellular  
1079 immunity and increases infectivity. *Cell Host Microbe* **29**, 1124-1136,  
1080 doi:10.1016/j.chom.2021.06.006 (2021).
- 1081 23 Saito, A. *et al.* Enhanced fusogenicity and pathogenicity of SARS-CoV-2  
1082 Delta P681R mutation. *Nature*, doi:10.1038/s41586-021-04266-9 (2021).
- 1083 24 Kimura, I. *et al.* The SARS-CoV-2 Lambda variant exhibits enhanced  
1084 infectivity and immune resistance. *Cell Rep*, doi:  
1085 <https://doi.org/10.1016/j.celrep.2021.110218> (2021).
- 1086 25 Schubert, M. *et al.* Human serum from SARS-CoV-2 vaccinated and  
1087 COVID-19 patients shows reduced binding to the RBD of SARS-CoV-2  
1088 Omicron variant. *MedRxiv*, doi:  
1089 <https://doi.org/10.1101/2021.1112.1110.21267523> (2022).
- 1090 26 Wu, L. *et al.* SARS-CoV-2 Omicron RBD shows weaker binding affinity  
1091 than the currently dominant Delta variant to human ACE2. *Signal*  
1092 *Transduct Target Ther* **7**, 8, doi:10.1038/s41392-021-00863-2 (2022).
- 1093 27 Mlcochova, P. *et al.* SARS-CoV-2 B.1.617.2 Delta variant replication and

- 1094 immune evasion. *Nature* **599**, 114-119, doi:10.1038/s41586-021-03944-y  
1095 (2021).
- 1096 28 Chen, S., Zhou, Y., Chen, Y. & Gu, J. fastp: an ultra-fast all-in-one  
1097 FASTQ preprocessor. *Bioinformatics* **34**, i884-i890,  
1098 doi:10.1093/bioinformatics/bty560 (2018).
- 1099 29 Matsuyama, S. *et al.* Enhanced isolation of SARS-CoV-2 by  
1100 TMPRSS2-expressing cells. *Proc Natl Acad Sci U S A* **117**, 7001-7003,  
1101 doi:10.1073/pnas.2002589117 (2020).
- 1102 30 Li, H. & Durbin, R. Fast and accurate short read alignment with  
1103 Burrows-Wheeler transform. *Bioinformatics* **25**, 1754-1760,  
1104 doi:10.1093/bioinformatics/btp324 (2009).
- 1105 31 Li, H. *et al.* The Sequence Alignment/Map format and SAMtools.  
1106 *Bioinformatics* **25**, 2078-2079, doi:10.1093/bioinformatics/btp352 (2009).
- 1107 32 Cingolani, P. *et al.* A program for annotating and predicting the effects of  
1108 single nucleotide polymorphisms, SnpEff: SNPs in the genome of  
1109 *Drosophila melanogaster* strain w1118; iso-2; iso-3. *Fly (Austin)* **6**, 80-92,  
1110 doi:10.4161/fly.19695 (2012).
- 1111 33 Li, H. Minimap2: pairwise alignment for nucleotide sequences.  
1112 *Bioinformatics* **34**, 3094-3100, doi:10.1093/bioinformatics/bty191 (2018).
- 1113 34 Capella-Gutierrez, S., Silla-Martinez, J. M. & Gabaldon, T. trimAl: a tool  
1114 for automated alignment trimming in large-scale phylogenetic analyses.  
1115 *Bioinformatics* **25**, 1972-1973, doi:10.1093/bioinformatics/btp348 (2009).
- 1116 35 Stamatakis, A. RAxML version 8: a tool for phylogenetic analysis and  
1117 post-analysis of large phylogenies. *Bioinformatics* **30**, 1312-1313,  
1118 doi:10.1093/bioinformatics/btu033 (2014).
- 1119 36 Bouckaert, R. *et al.* BEAST 2: a software platform for Bayesian  
1120 evolutionary analysis. *PLoS Comput Biol* **10**, e1003537,  
1121 doi:10.1371/journal.pcbi.1003537 (2014).
- 1122 37 Hasegawa, M., Kishino, H. & Yano, T. Dating of the human-ape splitting  
1123 by a molecular clock of mitochondrial DNA. *J Mol Evol* **22**, 160-174,  
1124 doi:10.1007/BF02101694 (1985).
- 1125 38 Vohringer, H. S. *et al.* Genomic reconstruction of the SARS-CoV-2  
1126 epidemic in England. *Nature* **600**, 506-511,  
1127 doi:10.1038/s41586-021-04069-y (2021).
- 1128 39 Obermeyer, F. *et al.* Analysis of 2.1 million SARS-CoV-2 genomes  
1129 identifies mutations associated with transmissibility. *MedRxiv*, doi:  
1130 <https://doi.org/10.1101/2021.1109.1107.21263228> (2022).
- 1131 40 Yamamoto, M. *et al.* The Anticoagulant Nafamostat Potently Inhibits  
1132 SARS-CoV-2 S Protein-Mediated Fusion in a Cell Fusion Assay System  
1133 and Viral Infection In Vitro in a Cell-Type-Dependent Manner. *Viruses* **12**,  
1134 doi:10.3390/v12060629 (2020).

- 1135 41 Ozono, S. *et al.* SARS-CoV-2 D614G spike mutation increases entry  
1136 efficiency with enhanced ACE2-binding affinity. *Nat Commun* **12**, 848,  
1137 doi:10.1038/s41467-021-21118-2 (2021).
- 1138 42 Liu, Y. *et al.* The SARS-CoV-2 Delta variant is poised to acquire complete  
1139 resistance to wild-type spike vaccines. *BioRxiv*, doi:  
1140 <https://doi.org/10.1101/2021.1108.1122.457114> (2021).
- 1141 43 Uriu, K. *et al.* Neutralization of the SARS-CoV-2 Mu Variant by  
1142 Convalescent and Vaccine Serum. *N Engl J Med* **385**, 2397-2399,  
1143 doi:10.1056/NEJMc2114706 (2021).
- 1144 44 Ozono, S., Zhang, Y., Tobiume, M., Kishigami, S. & Tokunaga, K.  
1145 Super-rapid quantitation of the production of HIV-1 harboring a  
1146 luminescent peptide tag. *J Biol Chem* **295**, 13023-13030,  
1147 doi:10.1074/jbc.RA120.013887 (2020).
- 1148 45 Reed, L. J. & Muench, H. A Simple Method of Estimating Fifty Percent  
1149 Endpoints. *Am J Hygiene* **27**, 493-497 (1938).
- 1150 46 Zahradnik, J. *et al.* A Protein-Engineered, Enhanced Yeast Display  
1151 Platform for Rapid Evolution of Challenging Targets. *ACS Synth Biol* **10**,  
1152 3445-3460, doi:10.1021/acssynbio.1c00395 (2021).
- 1153 47 Zahradnik, J. *et al.* SARS-CoV-2 variant prediction and antiviral drug  
1154 design are enabled by RBD in vitro evolution. *Nat Microbiol* **6**, 1188-1198,  
1155 doi:10.1038/s41564-021-00954-4 (2021).
- 1156 48 Peleg, Y. & Unger, T. Application of the restriction-free (RF) cloning for  
1157 multicomponents assembly. *Methods Mol Biol* **1116**, 73-87,  
1158 doi:10.1007/978-1-62703-764-8\_6 (2014).
- 1159  
1160



1161 **Author Contributions**

1162 Daichi Yamasoba, Izumi Kimura, Hesham Nasser, Keiya Uriu, Kotaro Shirakawa,  
1163 Yusuke Kosugi, Mako Toyoda, Yuri L Tanaka, Erika P Butlertanaka, Ryo  
1164 Shimizu, Kayoko Nagata, Takamasa Ueno, Akatsuki Saito, Takashi Irie,  
1165 Terumasa Ikeda, Kei Sato performed cell culture experiments.

1166 Jiri Zahradnik, Gideon Schreiber performed an yeast surface display assay.

1167 Yuhei Morioka, Naganori Nao, Rigel Suzuki, Mai Kishimoto, Kouji Kobiyama,  
1168 Teppei Hara, Hayato Ito, Yasuko Orba, Michihito Sasaki, Kumiko Yoshimatsu,  
1169 Ken J Ishii, Hirofumi Sawa, Keita Matsuno, Takasuke Fukuhara performed  
1170 animal experiments.

1171 Masumi Tsuda, Lei Wang, Yoshitaka Oda, Shinya Tanaka performed  
1172 histopathological analysis.

1173 Hiroyuki Asakura, Mami Nagashima, Kenji Sadamasu, Kazuhisa Yoshimura  
1174 performed viral genome sequencing analysis.

1175 Kotaro Shirakawa, Jin Kuramochi, Motoaki Seki, Ryoji Fujiki, Atsushi Kaneda,  
1176 Tadanaga Shimada, Taka-aki Nakada, Seiichiro Sakao, Takuji Suzuki, Akifumi  
1177 Takaori-Kondo contributed clinical sample collection.

1178 Jumpei Ito performed statistical, modelling, and bioinformatics analyses.

1179 Jumpei Ito, Akatsuki Saito, Takashi Irie, Shinya Tanaka, Keita Matsuno,  
1180 Takasuke Fukuhara, Terumasa Ikeda, and Kei Sato designed the experiments  
1181 and interpreted the results.

1182 Jumpei Ito and Kei Sato wrote the original manuscript.

1183 All authors reviewed and proofread the manuscript.

1184 The Genotype to Phenotype Japan (G2P-Japan) Consortium contributed to the  
1185 project administration.

1186

1187 **Conflict of interest**

1188 The authors declare that no competing interests exist.

1189

1190 **Acknowledgments**

1191 We would like to thank all members belonging to The Genotype to Phenotype  
1192 Japan (G2P-Japan) Consortium. We thank Dr. Kenzo Tokunaga (National  
1193 Institute for Infectious Diseases, Japan) and Dr. Jin Gohda (The University of  
1194 Tokyo, Japan) and Dr. Hisashi Arase (Osaka University) for providing reagents.  
1195 The super-computing resource was provided by Human Genome Center at The  
1196 University of Tokyo.

1197 This study was supported in part by AMED Research Program on  
1198 Emerging and Re-emerging Infectious Diseases (20fk0108268, to Akifumi  
1199 Takaori-Kondo; 20fk0108517, to Akifumi Takaori-Kondo; 20fk0108401, to  
1200 Takasuke Fukuhara; 20fk010847, to Takasuke Fukuhara; 21fk0108617 to  
1201 Takasuke Fukuhara; 20fk0108146, to Kei Sato; 20fk0108270, to Kei Sato; and

1202 20fk0108413, to Atsushi Kaneda, Terumasa Ikeda and Kei Sato) and  
1203 (20fk0108451, to G2P-Japan Consortium, Akatsuki Saito, Takashi Irie, Keita  
1204 Matsuno, Takasuke Fukuhara, Terumasa Ikeda, and Kei Sato); AMED Research  
1205 Program on HIV/AIDS (21fk0410034, to Akifumi Takaori-Kondo; 21fk0410033,  
1206 to Akatsuki Saito; and 21fk0410039, to Kei Sato); AMED CRDF Global Grant  
1207 (21jk0210039 to Akatsuki Saito); AMED Japan Program for Infectious Diseases  
1208 Research and Infrastructure (21wm0325009, to Akatsuki Saito; 21wm0125008,  
1209 to Hirofumi Sawa and 21wm0225003, to Hirofumi Sawa); JST A-STEP  
1210 (JPMJTM20SL, to Terumasa Ikeda); JST SICORP (e-ASIA) (JPMJSC20U1, to  
1211 Kei Sato); JST SICORP (JPMJSC21U5, to Kei Sato), JST CREST  
1212 (JPMJCR20H4, to Kei Sato); JSPS KAKENHI Grant-in-Aid for Scientific  
1213 Research C (19K06382, to Akatsuki Saito); JSPS KAKENHI Grant-in-Aid for  
1214 Scientific Research B (21H02736, to Takasuke Fukuhara; 18H02662, to Kei  
1215 Sato; and 21H02737, to Kei Sato); JSPS Fund for the Promotion of Joint  
1216 International Research (Fostering Joint International Research) (18KK0447, to  
1217 Kei Sato); JSPS Core-to-Core Program (A. Advanced Research Networks)  
1218 (JPJSCCA20190008, to Kei Sato); JSPS Research Fellow DC1 (19J20488, to  
1219 Izumi Kimura); JSPS Leading Initiative for Excellent Young Researchers  
1220 (LEADER) (to Terumasa Ikeda); World-leading Innovative and Smart Education  
1221 (WISE) Program 1801 from the Ministry of Education, Culture, Sports, Science  
1222 and Technology (MEXT) (to Naganori Nao); The Tokyo Biochemical Research  
1223 Foundation (to Kei Sato); Mitsubishi Foundation (to Terumasa Ikeda);  
1224 Shin-Nihon Foundation of Advanced Medical Research (to Mako Toyoda and  
1225 Terumasa Ikeda); Tsuchiya Foundation (to Takashi Irie); a Grant for Joint  
1226 Research Projects of the Research Institute for Microbial Diseases, Osaka  
1227 University (to Akatsuki Saito); an intramural grant from Kumamoto University  
1228 COVID-19 Research Projects (AMABIE) (to Terumasa Ikeda); Intercontinental  
1229 Research and Educational Platform Aiming for Eradication of HIV/AIDS (to  
1230 Terumasa Ikeda); and Joint Usage/Research Center program of Institute for  
1231 Frontier Life and Medical Sciences, Kyoto University (to Kei Sato).

1232

## 1233 **Consortia**

### 1234 **The Genotype to Phenotype Japan (G2P-Japan) Consortium**

1235 Mai Suganami<sup>1</sup>, Akiko Oide<sup>1</sup>, Mika Chiba<sup>1</sup>, Tomokazu Tamura<sup>5</sup>, Kana Tsushima<sup>5</sup>,  
1236 Haruko Kubo<sup>5</sup>, Zannatul Ferdous<sup>9</sup>, Hiromi Mouri<sup>9</sup>, Miki Iida<sup>9</sup>, Keiko Kasahara<sup>9</sup>,  
1237 Koshiro Tabata<sup>9</sup>, Mariko Ishizuka<sup>9</sup>, Asako Shigeno<sup>29</sup>, Kenzo Tokunaga<sup>32</sup>, Seiya  
1238 Ozono<sup>32</sup>, Isao Yoshida<sup>21</sup>, So Nakagawa<sup>33</sup>, Jiaqi Wu<sup>33</sup>, Miyoko Takahashi<sup>33</sup>,  
1239 Bahityar Rahmutulla Nawaj<sup>23</sup>, Yutaka Suzuki<sup>34</sup>, Yukie Kashima<sup>34</sup>, Kazumi Abe<sup>34</sup>,  
1240 Kiyomi Imamura<sup>34</sup>, Ryoko Kawabata<sup>28</sup>, Otowa Takahashi<sup>3</sup>, Kimiko Ichihara<sup>3</sup>,  
1241 Kazuko Kitazato<sup>3</sup>, Haruyo Hasebe<sup>3</sup>, Chihiro Motozono<sup>17</sup>, Toong Seng Tan<sup>17</sup>,  
1242 Isaac Ngare<sup>17</sup>

1243

1244 <sup>32</sup> National Institute of Infectious Diseases, Tokyo, Japan

1245 <sup>33</sup> Tokai University, Isehara, Japan

1246 <sup>34</sup> The University of Tokyo, Kashiwa, Japan

1247

1248 **Figure legends**

1249

1250 **Fig. 1 | Epidemic of BA.2.**

1251 **a**, Maximum likelihood tree of the Omicron lineages sampled from South Africa.  
1252 Asterisk denote nodes with  $\geq 0.95$  bootstrap values. **b**, Number of amino acid  
1253 differences between viral lineages detected in S (filled) or the other regions  
1254 (opened). **c**, Relative frequency of BA.2 in the genome surveillance data during  
1255 January 2022. The values for the countries with  $\geq 20$  SARS-CoV-2 sequences  
1256 are shown. **d**, Estimated relative effective reproduction number of each viral  
1257 lineage, assuming a fixed generation time of 2.1 days. The global average value  
1258 estimated by a Bayesian hierarchical model is shown. The value in each country  
1259 is shown in **Extended Data Fig. 2d**. The posterior distribution (violin), 95% CI  
1260 (line), and posterior mean (dot) are shown.

1261

1262 **Fig. 2 | Immune resistance of BA.2.**

1263 **a**, Amino acid substitutions in S. Left, primary structure and respective domains.  
1264 Numbers indicate amino acid position. NTD, N-terminal domain; RBM,  
1265 receptor-binding motif; HR, heptad repeat; TMD, transmembrane domain. Right,  
1266 heatmap showing the frequency of amino acid substitutions. Substitutions  
1267 detected in  $>10\%$  sequences of any lineages are shown. **b–h**, Neutralisation  
1268 assays. Neutralisation assays were performed with the pseudoviruses  
1269 harbouring the S proteins of B.1.1 (the D614G-bearing ancestral virus), Delta,  
1270 BA.1 and BA.2. Vaccinated sera [**b**, mRNA-1273 (16 donors); **c**, ChAdOx1 (9  
1271 donors)], monoclonal antibodies (**d**), convalescent sera of the individuals  
1272 infected with early pandemic virus (until May 2020) (**e**, 12 donors), and BA.1 (**f**,  
1273 17 donors), convalescent sera of the hamsters infected B.1.1 (**g**, left; 6  
1274 hamsters) and BA.1 (**g**, right; 6 hamsters), and murine sera immunised with the  
1275 cells expressing B.1.1 S (**h**, left; 10 mice) and BA.1 S (**h**, right; 10 mice) were  
1276 used. In **b,c,e–h**, assay of each serum was performed in triplicate to determine  
1277 50% neutralisation titre (NT50). Each dot represents each NT50 value, and  
1278 geometric mean and 95% CI are shown. Number indicates the fold change of  
1279 resistance versus each antigenic variant. Statistically significant differences  
1280 between BA.1 and BA.2 were determined by two-sided Wilcoxon signed-rank  
1281 test. Information of vaccinated/convalescent donors are summarized in  
1282 **Supplementary Tables 1 and 2**. In **f**, the dots of not-fully vaccinated 4 donors  
1283 are filled. In **d**, assay of each concentration was performed in triplicate, and data  
1284 are the average  $\pm$  s.d. IC50, 50% inhibitory concentration; ND, not determined.

1285

1286 **Fig. 3 | Virological features of BA.2 in vitro.**

1287 **a,h**, Growth kinetics of SARS-CoV-2 variants. **b**, Fluorescence microscopy. GFP  
1288 area of infected VeroE6/TMPRSS2 cells at 48 h.p.i were measured. Numbers in

1289 the panel indicate the number of GFP-positive cells counted. **c**, Plaque assay.  
1290 Diameter of plaques (20 plaques per virus) are summarized. **d,f**, S-based fusion  
1291 assay. The fusion activity (arbitrary units) is shown. **e**, Western blot. Left,  
1292 representative blots of S-expressing cells. ACTB is an internal control. Right, the  
1293 ratio of S2 to the full-length S plus S2 proteins. **g**, Fold increase of pseudovirus  
1294 infectivity by TMPRSS2 expression. Assays were performed in quadruplicate  
1295 (**a,g,h**), octuplicate (**a**, most left) or triplicate (**d–f**) and data are the average  $\pm$  s.d.  
1296 Each dot indicates the result from an individual plaque (**c**) and an individual  
1297 replicate (**e,g**). In **b** and **c**, raw data are shown in **Extended Data Fig. 5 and 6**.  
1298 Statistically significant differences between BA.2 and other variants through  
1299 timepoints were determined by multiple regression (**a,d,f,h**). Familywise error  
1300 rates (FWERs) calculated using the Holm method are indicated in the figures.  
1301 Statistically significant differences between BA.1 and BA.2 were determined by  
1302 two-sided Mann–Whitney *U*-tests (**b,d**) or two-sided paired Student's *t*-tests (**e**).  
1303

1304 **Fig. 4 | Virological features of BA.2 in vivo.**

1305 Syrian hamsters were intranasally inoculated with B.1.1, BA.1 and BA.2. **a**, Body  
1306 weight, Penh, Rpef, SpO<sub>2</sub> values routinely measured. Hamsters of the same age  
1307 were intranasally inoculated with PBS (uninfected). **b**, Viral RNA load in the lung  
1308 hilum (left) and periphery (right). **c,d**, Percentage of N-positive cells in the whole  
1309 lobes of lung (**c**) and bronchiole in the frontal/upper lobe of lung (**d**) measured by  
1310 IHC. **e**, Histopathological scoring of lung lesions. Representative pathological  
1311 features are shown in our previous studies<sup>12,23</sup>. Data are the average (**a**, 6  
1312 hamsters per each group; **b–e**, 4 hamsters per each group)  $\pm$  s.e.m. In **a–c,e**,  
1313 statistically significant differences between BA.2 and other variants or uninfected  
1314 hamsters through timepoints were determined by multiple regression. The data  
1315 at 0 d.p.i. was excluded from the analyses. FWERs calculated using the Holm  
1316 method are indicated in the figures. In **d**, each dot indicates the result from an  
1317 individual hamster. In **c–e**, raw data are shown in **Extended Data Fig. 7 and 8**.

1318 **Extended Data**

1319

1320 **Extended Data Fig. 1. Estimated emergence dates of the Omicron lineages.**

1321 **a**, Phylodynamics of BA.1 (top), BA.2 (middle), and BA.3 (bottom) sampled by  
1322 January 26, 2022 in South Africa. All the BA.2 and BA.3 sequences and 200  
1323 randomly sampled BA.1 (including 20 BA.1.1) sequences were used. The  
1324 time-resolved trees were constructed by BEAST2. Regarding a node with  $\geq 0.95$   
1325 posterior value (denoted by an asterisk), the 95% CI of the divergence time is  
1326 shown. **b**, Estimated emergence dates of the Omicron lineages. The 95% CI  
1327 (error bar) and posterior mean (dot) are shown.

1328

1329 **Extended Data Fig. 2. Epidemic dynamics of SARS-CoV-2 lineages in**  
1330 **countries with the BA.2 epidemic.**

1331 **a**, Daily sequence frequency of each viral lineage in eleven countries where  
1332  $\geq 100$  BA.2 sequences have been reported by January 25, 2022. This data was  
1333 used as an input of a Bayesian hierarchical model to estimate the epidemic  
1334 dynamics.

1335 **b,c**, Epidemic dynamics of SARS-CoV-2 viral lineages. The observed daily  
1336 frequency (dot) and the dynamics estimated by the Bayesian model (posterior  
1337 mean; line) are shown. Additionally, 95% CI (**b**) and 90% prediction interval (**c**)  
1338 are shown. **d**, Estimated relative effective reproduction number of each viral  
1339 lineage in each country. The posterior distribution (violin), 95% CI (line), and  
1340 posterior mean (dot) are shown.

1341

1342 **Extended Data Fig. 3. Immune resistance of BA.2.**

1343 Neutralisation assays were performed with the pseudoviruses harbouring the S  
1344 proteins of B.1.1 (the D614G-bearing ancestral virus), Alpha, Delta, BA.1 and  
1345 BA.2. Assay of each serum sample was performed in triplicate to determine  
1346 NT50, and each dot represents each NT50 value. Geometric mean and 95% CI  
1347 are shown. The number indicates the fold change of resistance versus each  
1348 antigenic variant. In **a** and **b**, statistically significant differences between BA.1  
1349 and BA.2 were determined by two-sided Wilcoxon signed-rank test. In **c**,  
1350 statistically significant differences between fully-vaccinated (13 donors) and  
1351 not-fully-vaccinated (4 donors) were determined by two-sided Mann-Whitney  
1352 U-test. Information of vaccinated and convalescent donors are summarized in  
1353 **Supplementary Tables 1 and 2**, respectively.

1354

1355 **Extended Data Fig. 4. Scheme of chimeric recombinant SARS-CoV-2 used**  
1356 **in this study.**

1357 The SARS-CoV-2 genome and respective genes are shown. The template is  
1358 SARS-CoV-2 strain WK-521 (lineage A, GISAID ID: EPI\_ISL\_408667), and the

1359 S genes were swapped with respective lineage/strain (GISAID IDs are indicated  
1360 in the figure). Additionally, the *ORF7b* was swapped with *sfGFP* gene.

1361

1362 **Extended Data Fig. 5. Syncytia and plaque formations by BA.2.**

1363 **a**, Fluorescence microscopy. GFP area of infected VeroE6/TMPRSS2 cells  
1364 (m.o.i. 0.01) at 24, 48, and 72 h.p.i were measured. Higher-magnification views  
1365 of the regions indicated by squares are shown at bottom. **b**, Plaque assay. **c**,  
1366 Coculture of S-expressing cells with HEK293-ACE2/TMPRSS2 cells. Left,  
1367 representative images of S-expressing cells cocultured with HEK293 cells (top)  
1368 or HEK293-ACE2/TMPRSS2 cells (bottom). Nuclei were stained with Hoechst  
1369 33342 (blue). Right, the size distribution of syncytia (green). Numbers in the  
1370 panel indicate the numbers of GFP-positive syncytia counted. Data are the  
1371 average  $\pm$  s.d. A statistically significant difference between BA.1 and BA.2 was  
1372 determined by two-sided Mann–Whitney *U*-test. In **a** and **b**, summarized data  
1373 are shown in **Fig. 3b** and **3c**. Scale bars, 500  $\mu$ m (**a**) or 200  $\mu$ m (**c**).

1374

1375 **Extended Data Fig. 6. Expression and binding properties of BA.2 S.**

1376 **a**, S expression on the cell surface. Representative histograms stained with  
1377 anti-S1/S2 polyclonal antibody (left) and the summarised data (right) are  
1378 respectively shown. The number in the histogram indicates MFI. Grey  
1379 histograms indicate isotype controls. **b**, Binding affinity of SARS-CoV-2 S RBD  
1380 to ACE2 by yeast surface display. Left, The percentage of the binding of the  
1381 SARS-CoV-2 S RBD expressed on yeast to soluble ACE2 (left) and the  
1382 summarised data (right) are respectively shown. **c**, TMPRSS2 expression on the  
1383 cell surface. Left, representative histograms stained with anti-TMPRSS2  
1384 polyclonal antibody are shown. The number in the histogram indicates MFI. Grey  
1385 histograms indicate isotype controls. Right, summarized data. Assays were  
1386 performed in triplicate, and data are the average  $\pm$  s.d. Each dot indicates the  
1387 result from an individual replicate. A statistically significant difference between  
1388 BA.1 and BA.2 was determined by two-sided unpaired Student's *t*-test (**a**) or  
1389 two-sided Mann–Whitney *U*-test (**b**).

1390

1391 **Extended Data Fig. 7. IHC of SARS-CoV-2 N protein.**

1392 **a,b**, IHC of viral N protein in the middle part of trachea of all infected hamsters ( $n$   
1393 = 4 per each viral strain) at 1 d.p.i. (**a**) and the lung at 1, 3 and 5 d.p.i. (**b**). Each  
1394 panel indicates the representative result from an individual infected hamster. **c**,  
1395 Lung lobes of the hamsters infected with B.1.1, BA.1 or BA.2 ( $n$  = 4 for each  
1396 virus) at 1, 3 and 5 d.p.i. were immunohistochemically stained with  
1397 anti-SARS-CoV-2 N monoclonal antibody. In each panel, IHC staining (top) and  
1398 the digitalized N-positive area (bottom, indicated in red) are shown. The number

1399 in the bottom panel indicates the percentage of N-positive area. Summarized  
1400 data is shown in **Fig. 4c**. Scale bars, 1 mm (**a**); 500  $\mu$ m (**b**); or 5 mm (**c**).

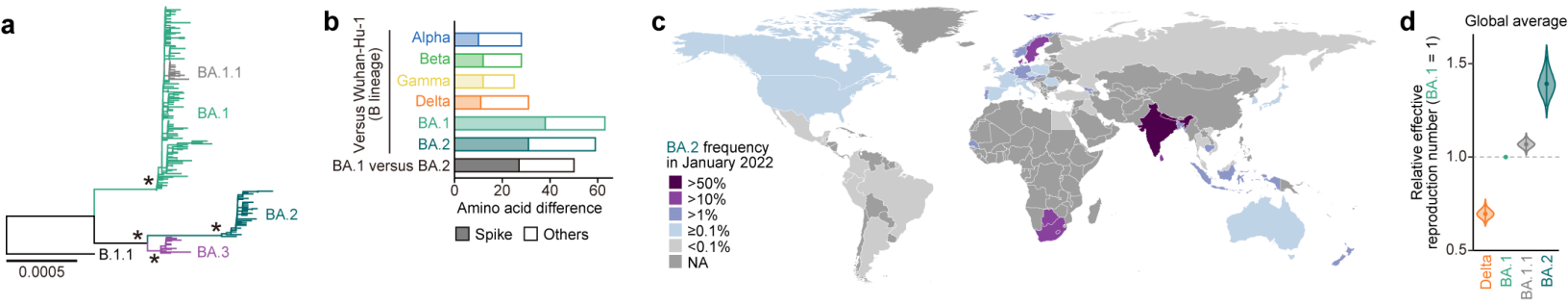
1401

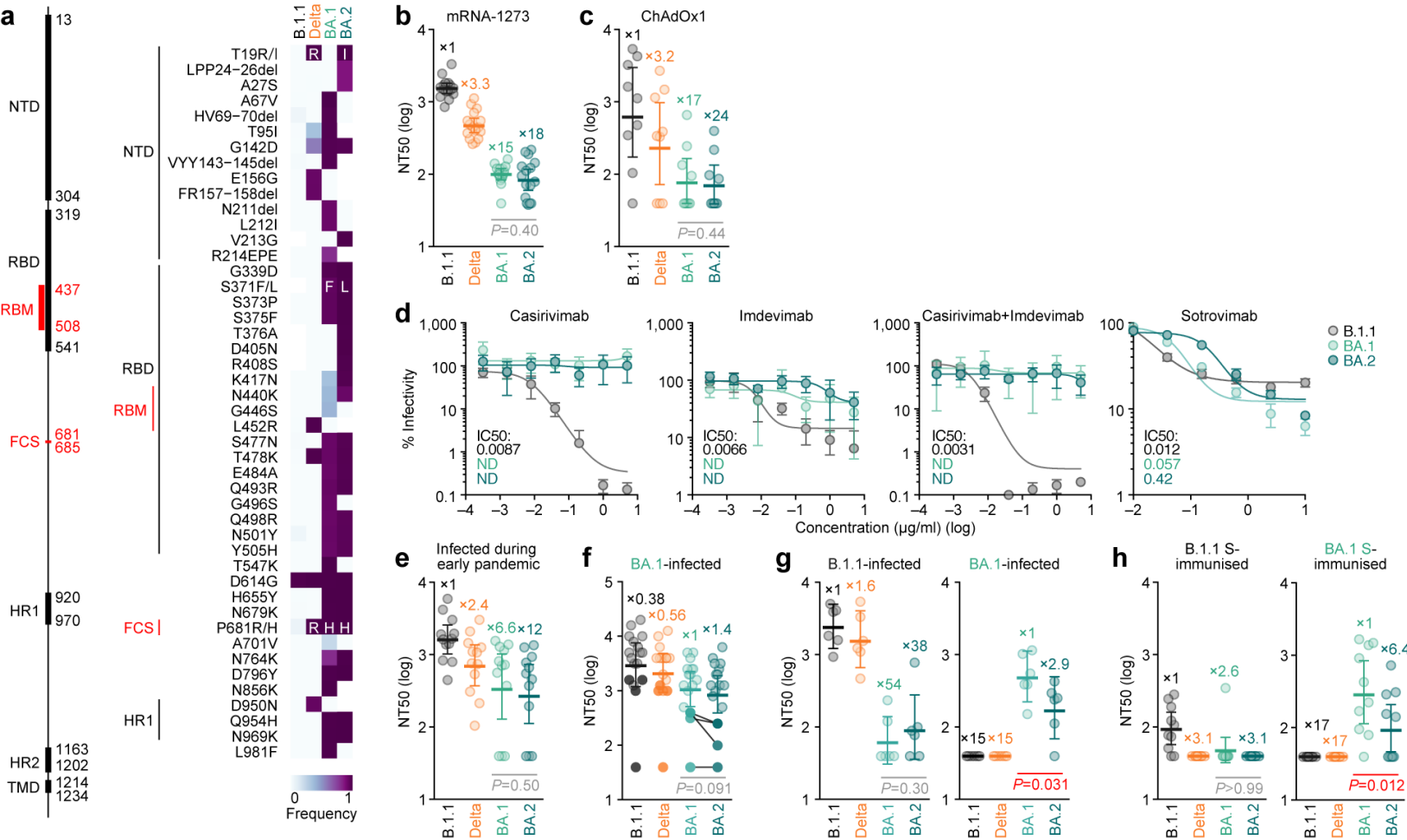
1402 **Extended Data Fig. 8. Pathological features of BA.2.**

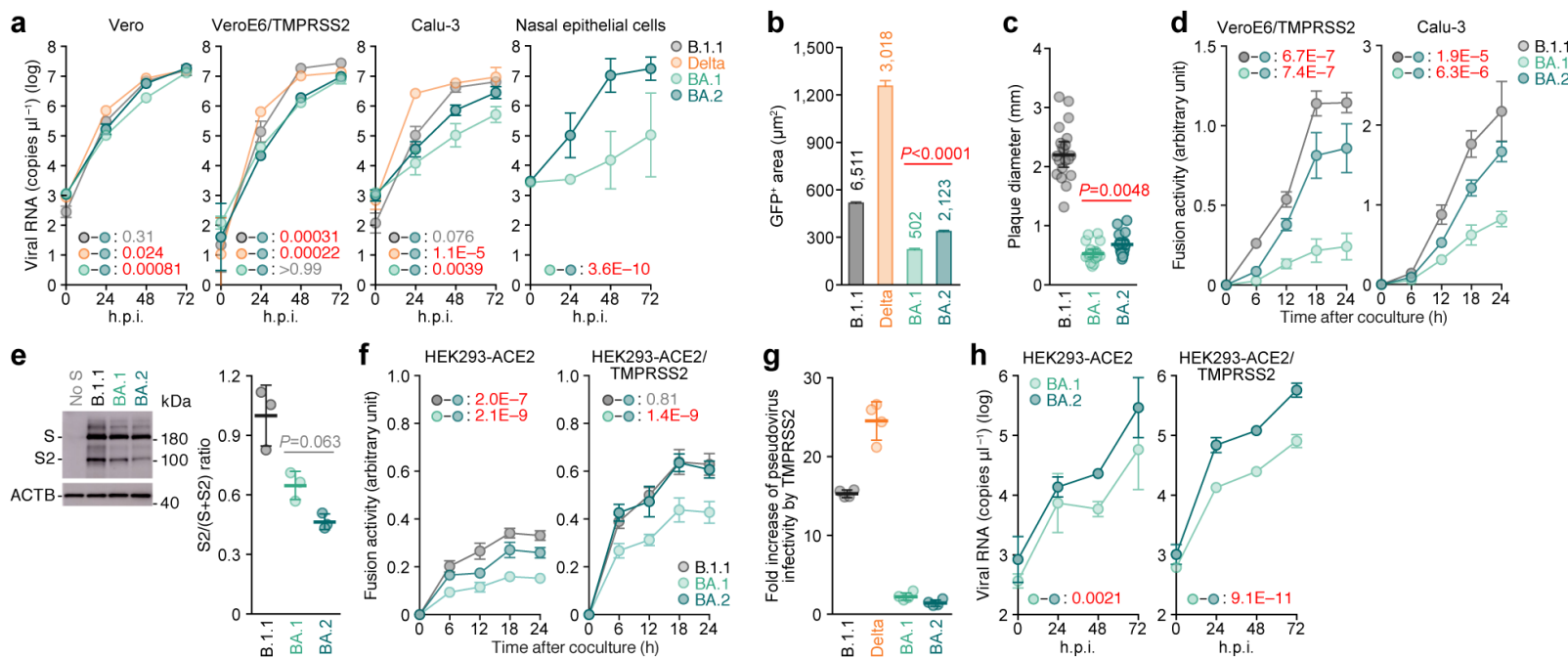
1403 **a**, H&E staining of the lungs of infected hamsters. Uninfected lung alveolar  
1404 space and bronchioles are also shown. **b**, Type II pneumocytes in the lungs of  
1405 infected hamsters. Left, lung lobes of the hamsters infected with B.1.1 (n = 4),  
1406 BA.1 (n = 4), and BA.2 (n = 4) at 5 d.p.i. In each panel, H&E staining (top) and  
1407 the digitalized inflammation area (bottom, indicated in red) are shown. The  
1408 number in the bottom panel indicates the percentage of the section represented  
1409 by the indicated area (i.e., the area indicated with red colour per the total area of  
1410 the lung lobes). Right, summarized data. Each dot indicates the result from an  
1411 individual hamster.

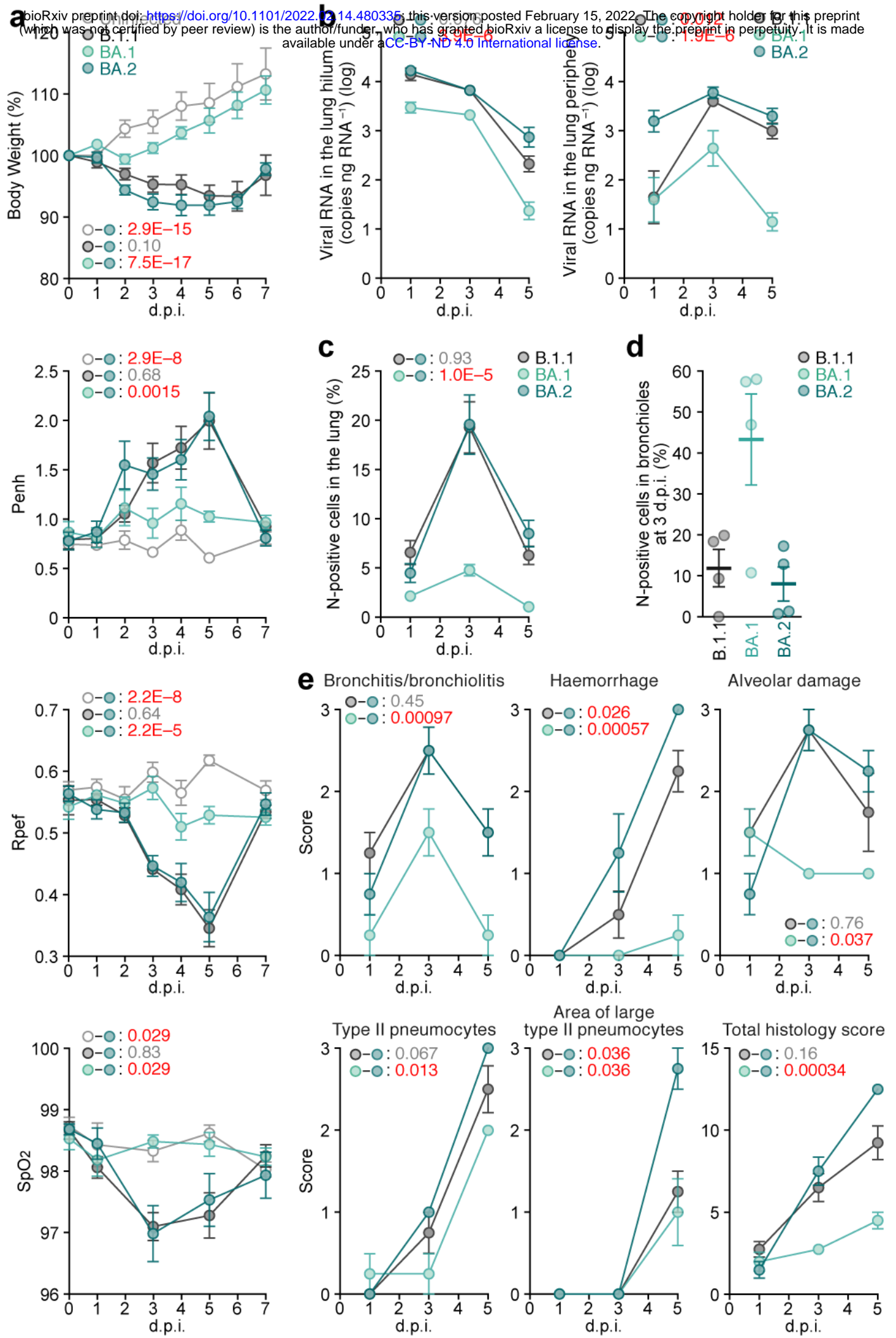
1412 Scale bars, 250  $\mu$ m (**a**) or 5 mm (**b**).





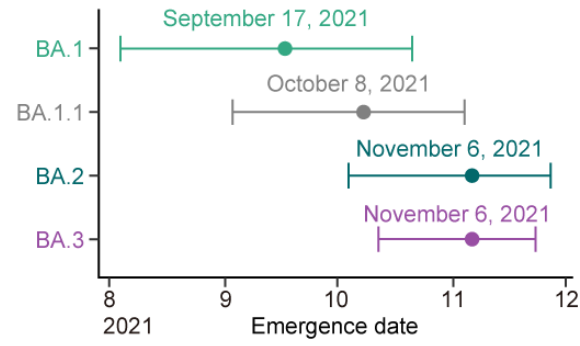
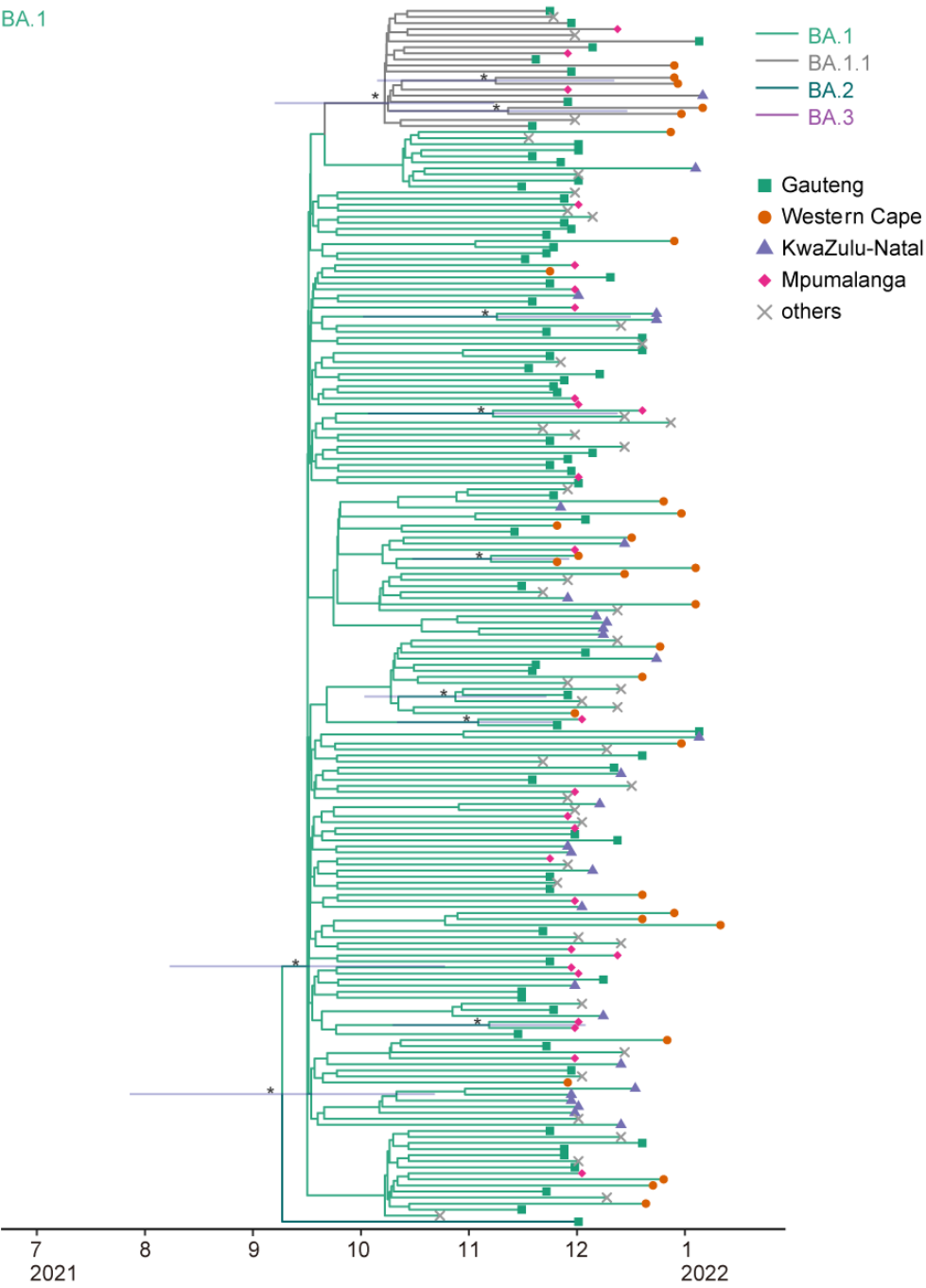




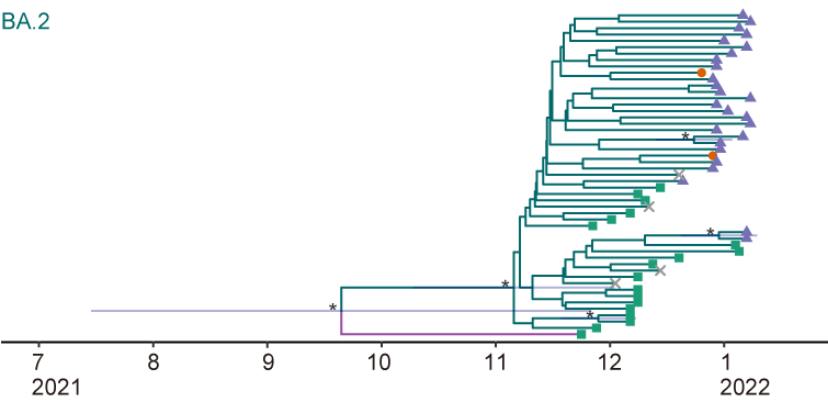


**a**

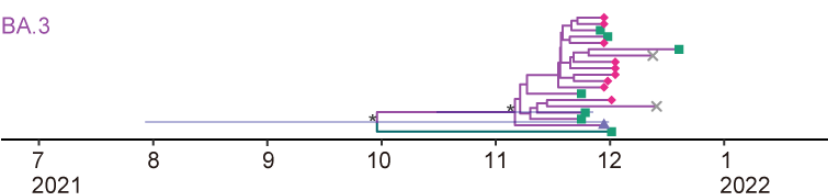
BA.1

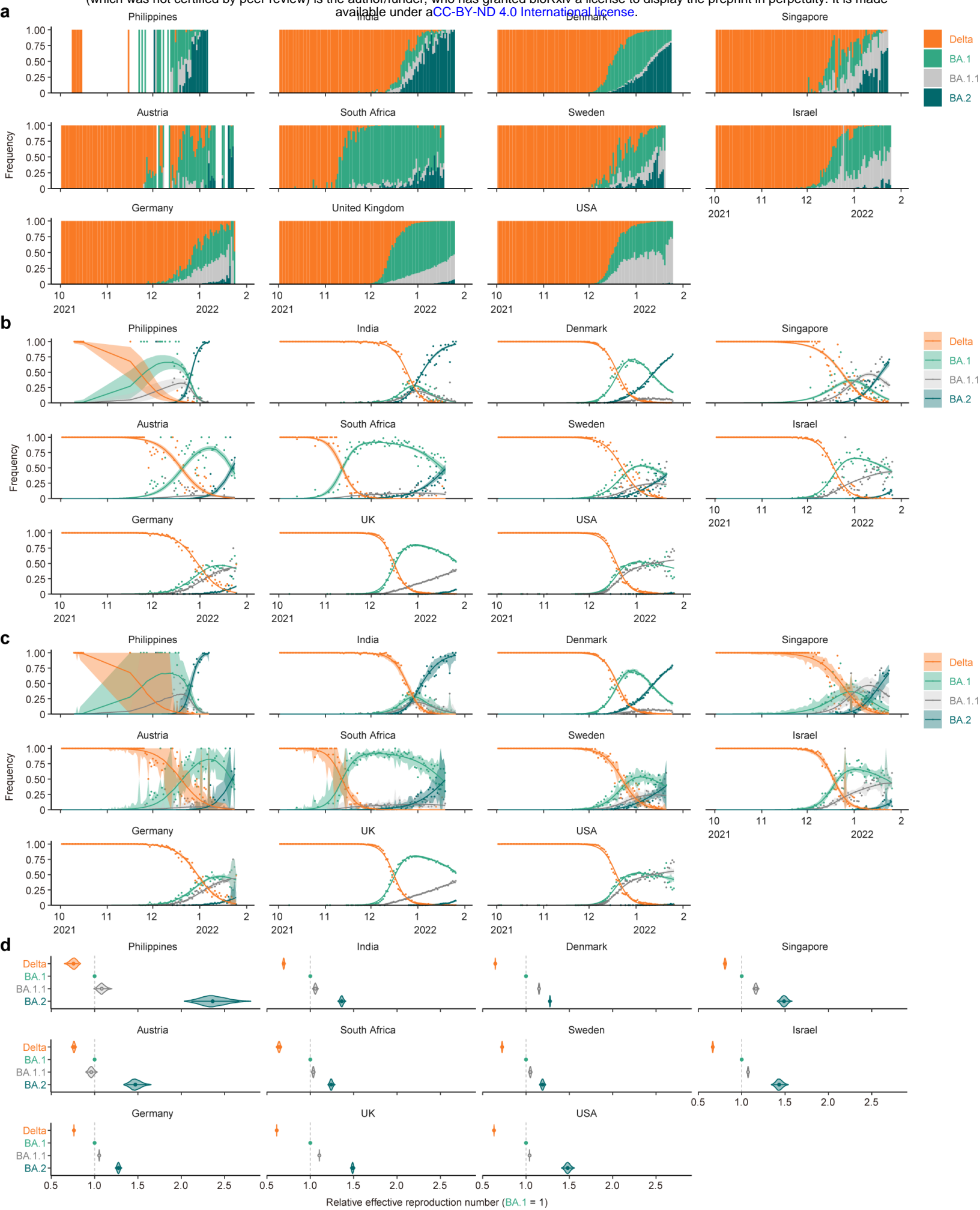


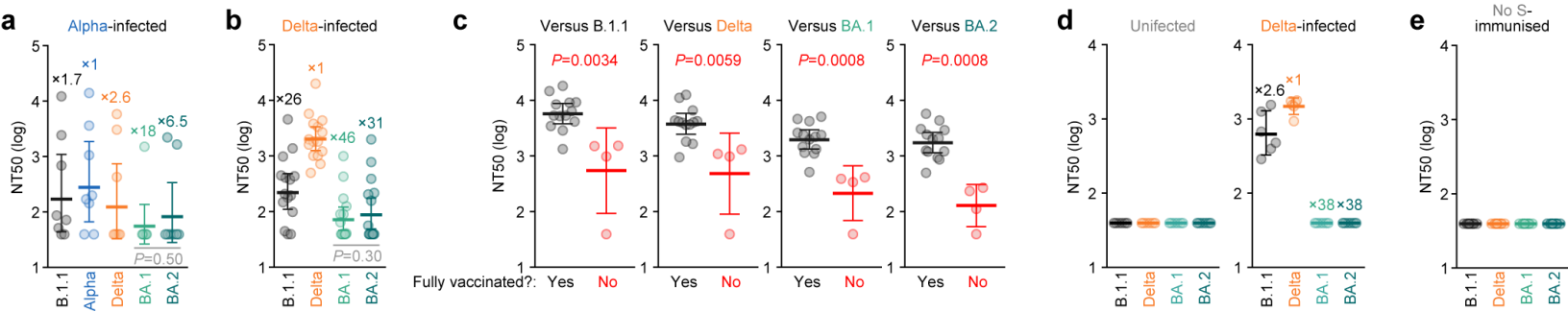
BA.2

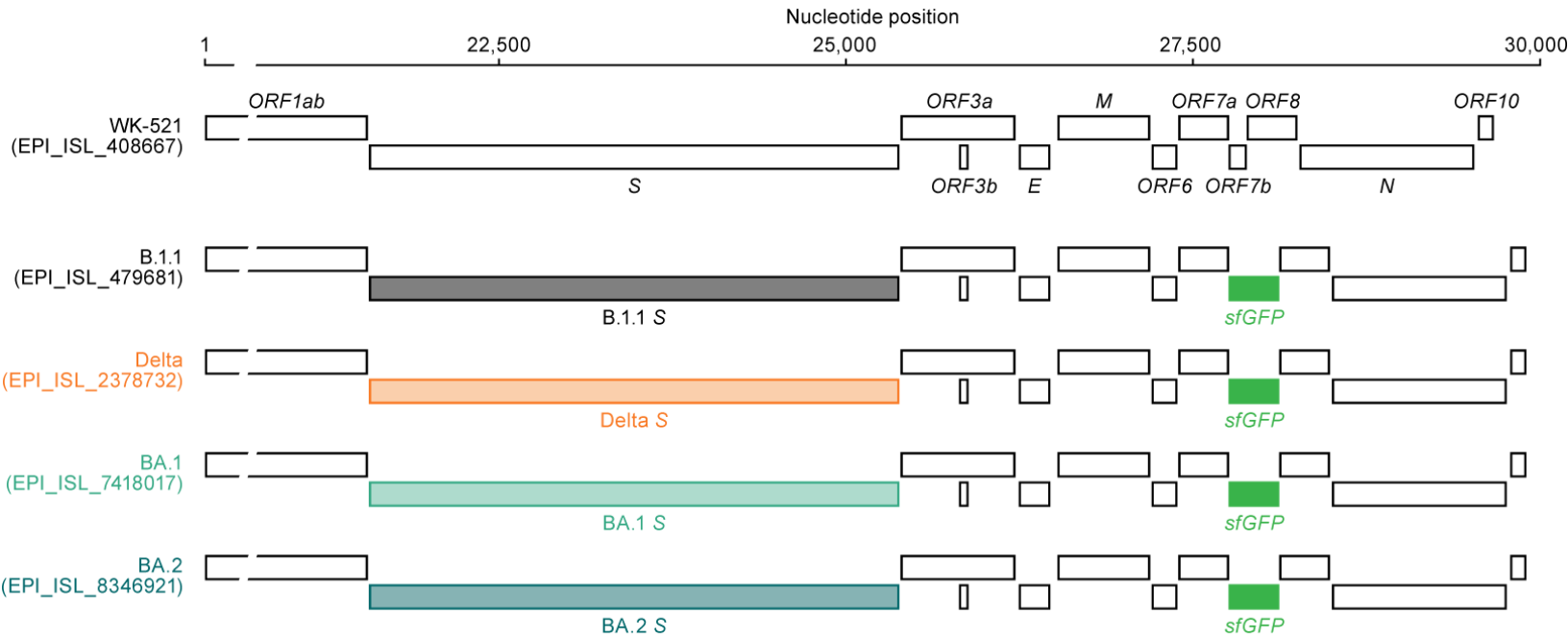


BA.3

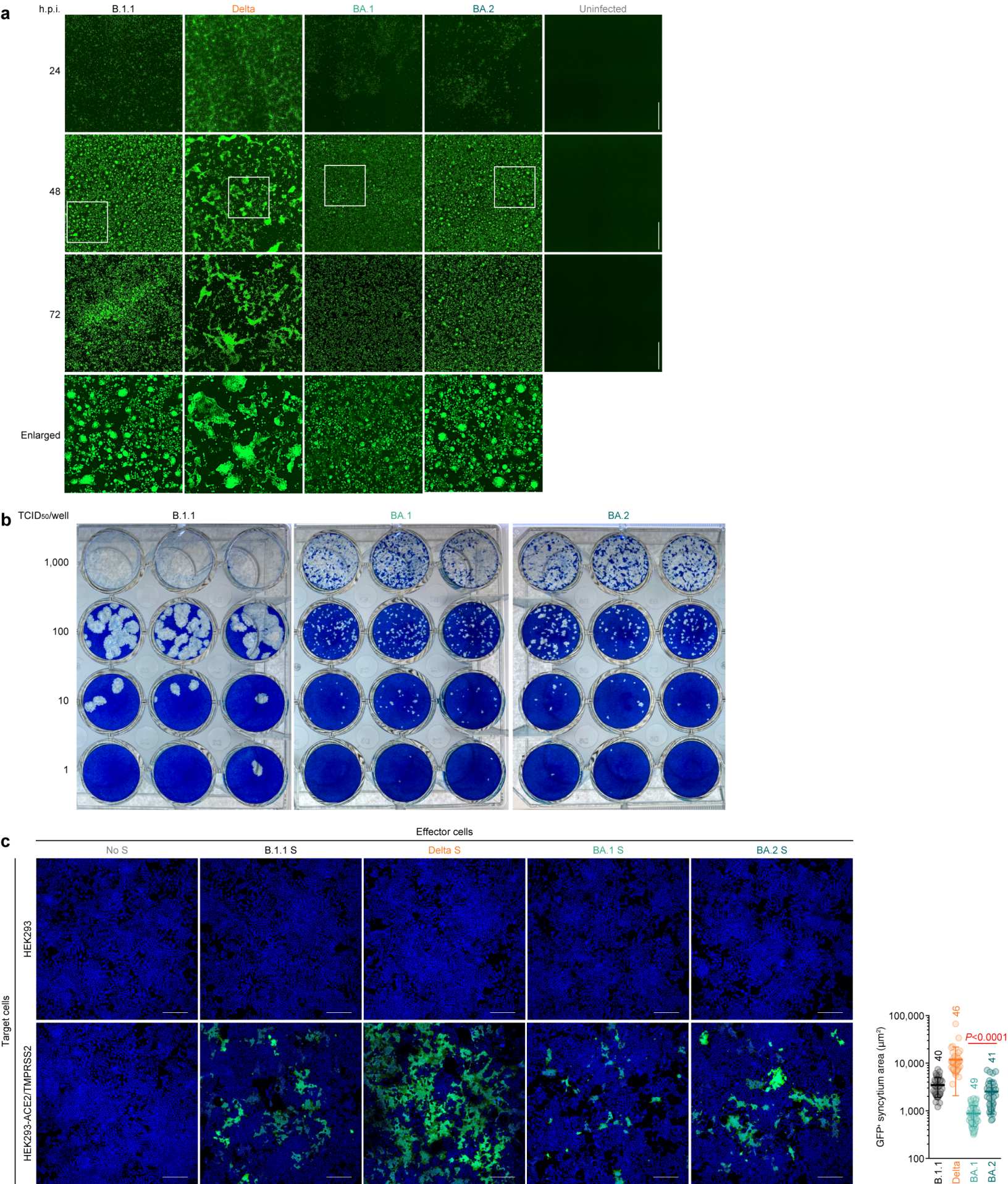


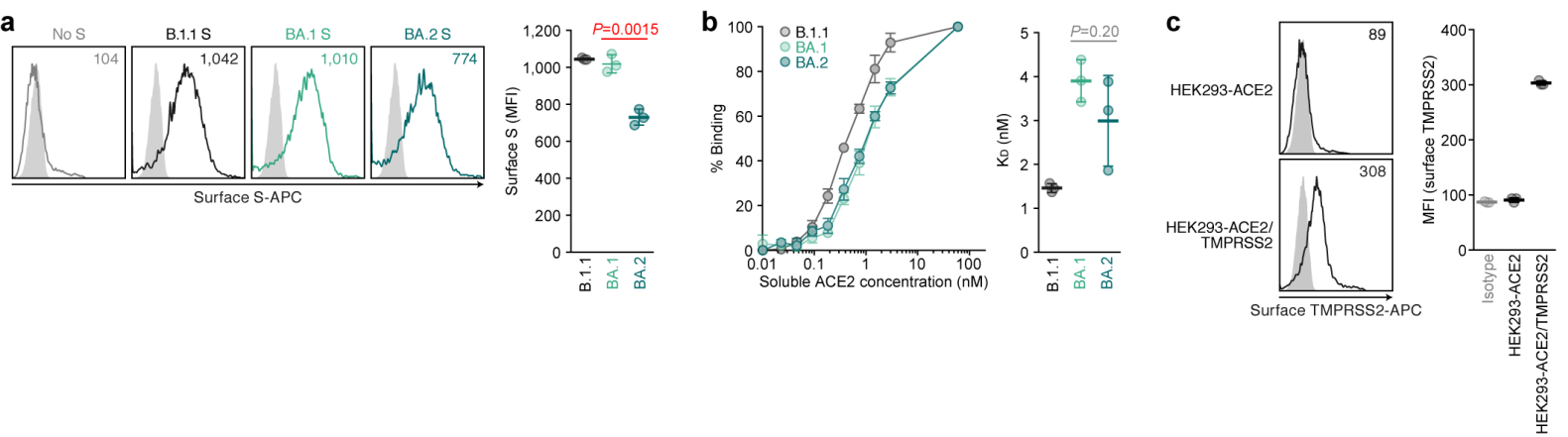


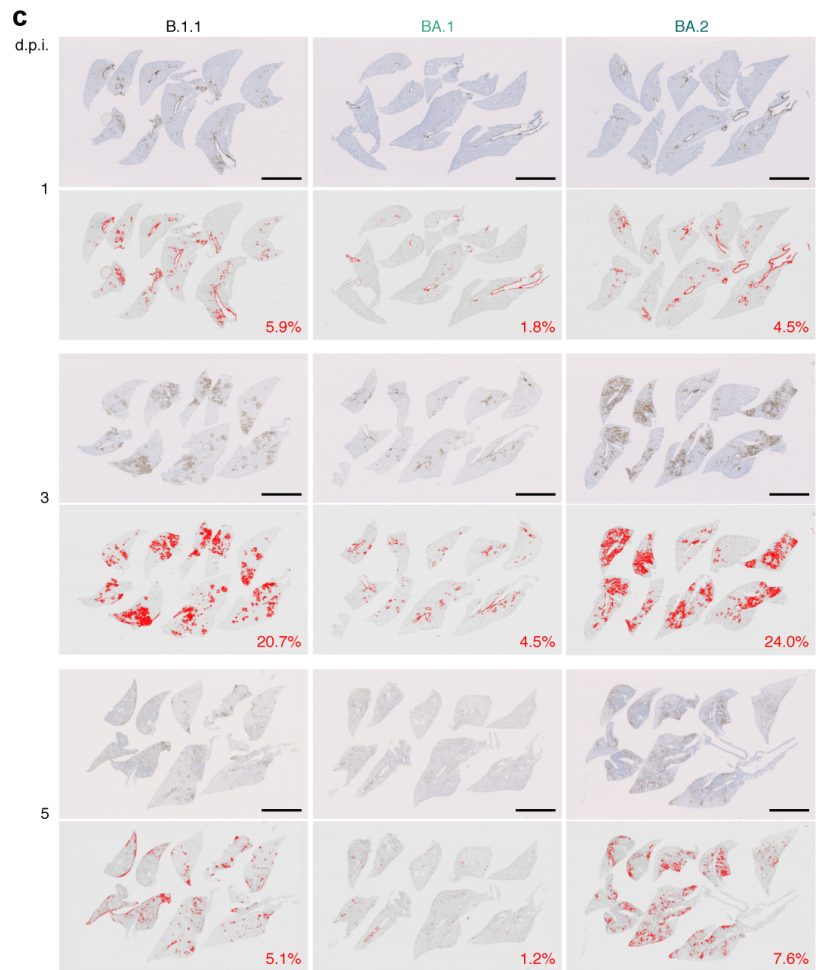
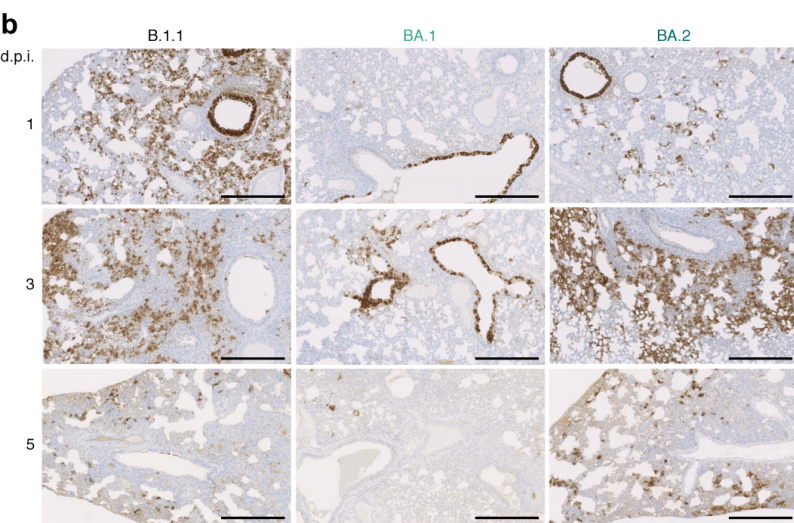
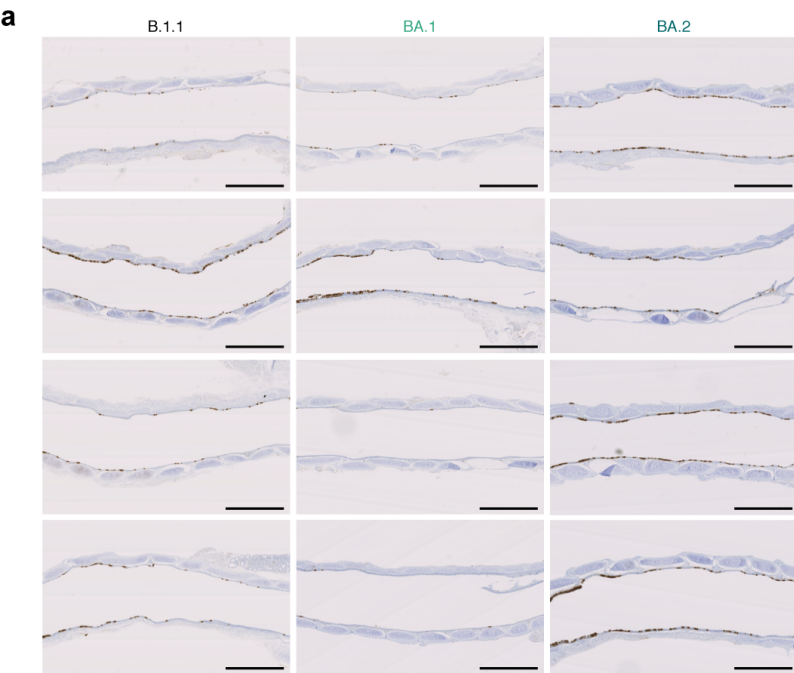




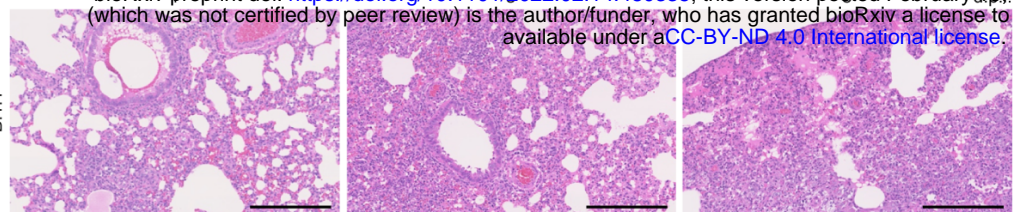




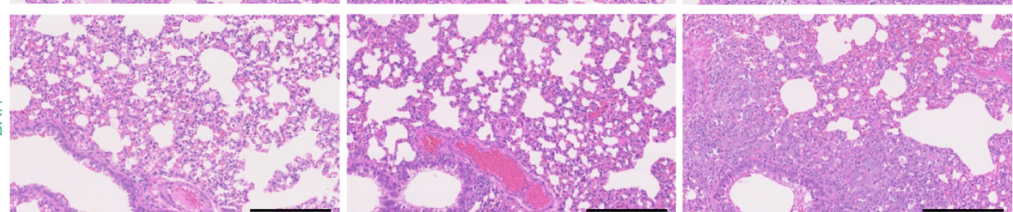




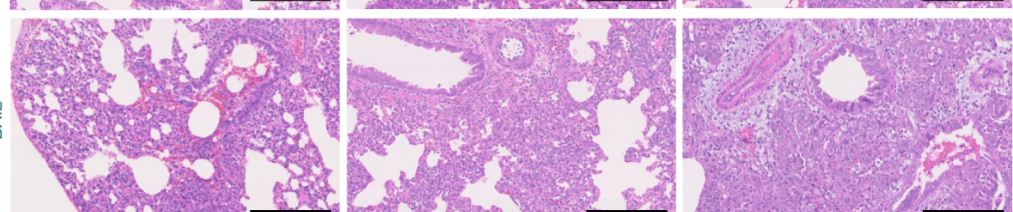
B.1.1



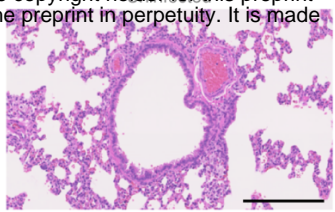
BA.1



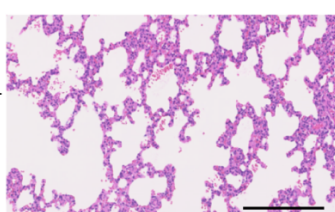
BA.2



Bronchiole

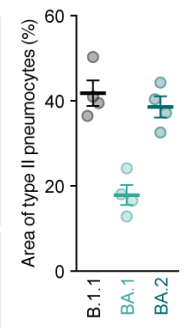
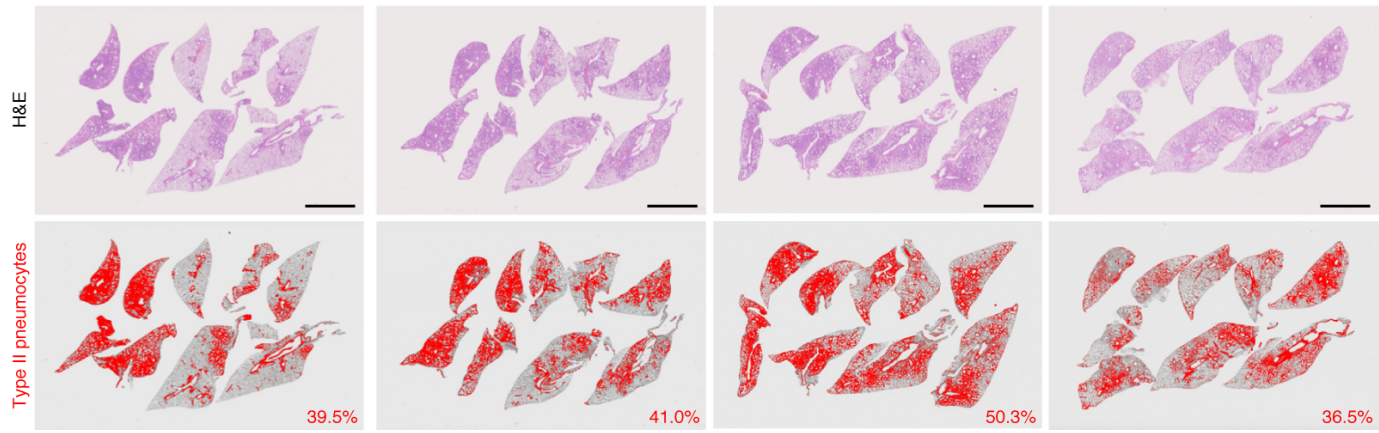


Alveolar space

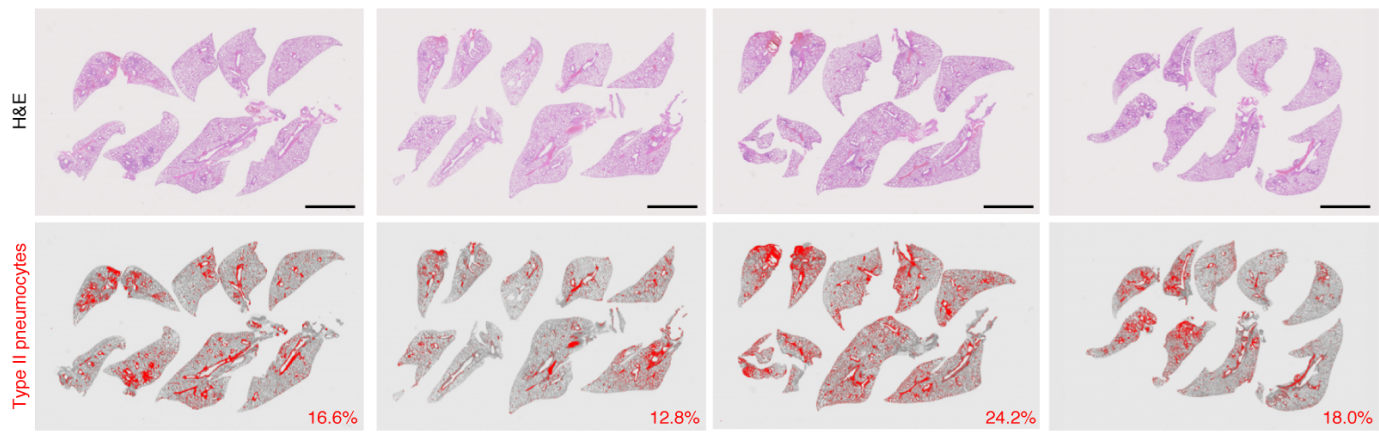


**b**

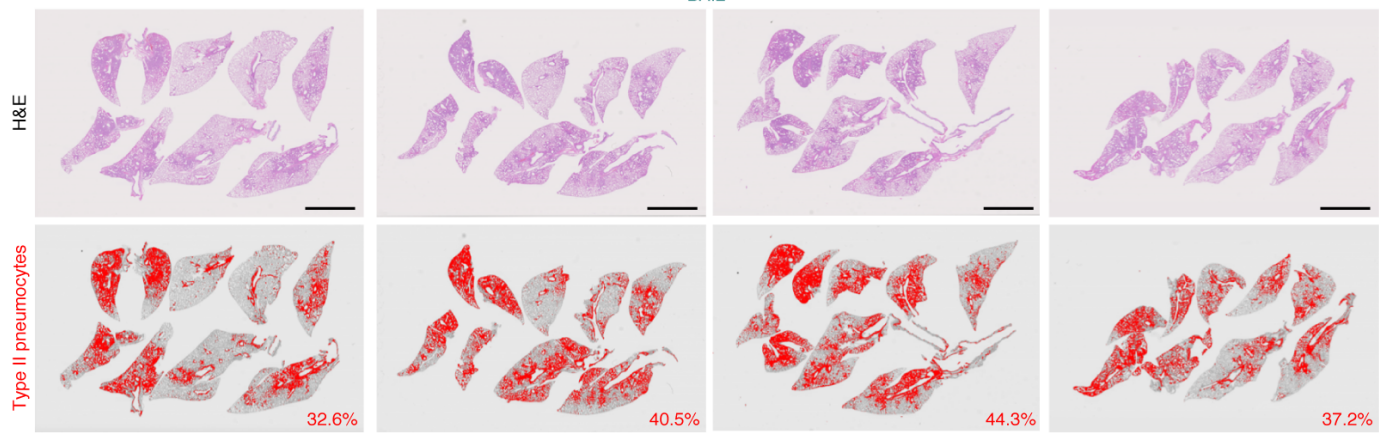
B.1.1



BA.1



BA.2



H&E

Type II pneumocytes

Area of type II pneumocytes (%)

B.1.1

BA.1

BA.2